FEBRUARY 2021 M.Sc. in Electrical and Electronics Engineering SEMIH BOYNO

REPUBLIC OF TURKEY

GAZİANTEP UNIVERSITY

GRADUATE SCHOOL OF NATURAL & APPLIED SCIENCES

SLIDING MODE ANTI-SWAY CONTROL AND DISTURBANCE REJECTION OF GANTRY CRANE

M.Sc. THESIS

IN

ELECTRICAL AND ELECTRONICS ENGINEERING

BY

SEMIH BOYNO

FEBRUARY 2021

SLIDING MODE ANTI-SWAY CONTROL AND DISTURBANCE REJECTION OF GANTRY CRANE

M.Sc. Thesis

in

Electrical and Electronics Engineering

Gaziantep University

Supervisor

Assoc. Prof. Dr. Tolgay KARA

by

Semih BOYNO

February 2021

I hereby declare that all information in this document has been obtained and presented in accordance with academic rules and ethical conduct. I also declare that, as required by these rules and conduct, I have fully cited and referenced all material and results that are not original to this work.

Semih BOYNO

ABSTRACT

SLIDING MODE ANTI-SWAY CONTROL AND DISTURBANCE REJECTION OF GANTRY CRANE

BOYNO, Semih

M.Sc. in Electrical and Electronics Engineering

Supervisor: Assoc. Prof. Dr. Tolgay KARA

February 2021

49 pages

In this study, a robust sliding mode control (SMC) strategy is suggested for suppression of load sway and rejection of disturbances in gantry cranes. First the dynamic model of gantry crane is derived from the general laws of motion and Lagrangian energy analysis. Then, a proper disturbance rejecting robust SMC mechanism with anti-sway property in conjunction with a Linear Quadratic Regulator (LQR) design is developed. Suggested control system is tested via computer simulations along with traditional Linear Quadratic Regulator (LQR) state feedback control and LQR with Proportional Integral Derivative (PID) control methods. The control simulation results of the crane dynamic model under ideal conditions without friction and actuators is compared. Simulation results reveal that suggested SMC strategy exhibits superior performance in suppressing sway and rejecting disturbances in gantry crane control.

Keywords: System Dynamics, PID Control, Sliding Mode Control, Anti-Sway, Disturbance Rejection, Gantry Crane

ÖZET

PORTAL VİNÇLERİN SALINIM ÖNLEYİCİ KAYAN KİPLİ KONTROLÜ VE BOZUNUMUN ENGELLENMESİ

BOYNO, Semih

Yüksek Lisans Tezi, Elektrik-Elektronik Mühendisliği

Danışman: Doç. Dr. Tolgay KARA

Şubat 2021

49 sayfa

Bu çalışmada, portal vinçlerde yük salınımının ve bozunumların engellenmesi için gürbüz kontrol sistemlerinden kayan kipli kontrol (SMC) stratejisi önerilmektedir. İlk olarak portal vincin matematiksel dinamitk denklemleri klasik fizik hareket kurallarından Lagrange yöntemiyle çıkarılmaktadır. Sonrasında, vinç sistemine uygun bozunum ve salınım engelleyici bir gürbüz SMC mekanizması doğrusal kuadratik regülatör (LQR) yardımıyla tasarlanmıştır. Önerilen SMC kontrol sistemi, sadece LQR ve doğrusal kuadratik regülatörlü PID (LQR-PID) kontrol sistemleriyle bilgisayar simülasyonu yapılarak karşılaştırılmıştır. Simülasyon esnasında sürtünme ve aktüatörlerin göz ardı edildiği ideal koşullarda yapılmıştır. Simülasyon sonuçlarına göre kayan kipli kontrol (SMC) stratejisi portal vinçlerde yük salınımını ve bozunumları engellemede diğer yöntemlere göre üstün performansa sahip olduğu belirlenmiştir.

Anahtar Kelimeler: Sistem Dinamiği, PID Kontrol, SMC Kontrol, Salınım Önleme, Bozunum Engelleme, Portal Vinç

I dedicate this thesis to my beloved family for their
continuous love, support and guidance,
and to my one and only beloved wife as she believed in me
and supported with great patience through my journey.

ACKNOWLEDGEMENTS

I would like to thank my supervisor Assoc. Prof. Dr. Tolgay KARA for his guidance and support throughout the study. I am thankful for his encouragement and motivation.
I also acknowledge and thank for the study materials my university have provided.
I would like to express my love and gratitude to my family for their continuous love, support and guidance.

TABLE OF CONTENTS

LIST OF TABLES

LIST OF FIGURES

LIST OF SYMBOLS

θ	Theta
η	Eta
σ	Sigma
ξ	Xi
°	Degree

LIST OF ABBREVIATIONS

LQR	Linear Quadratic Regulator
LTI	Linear Time Invariant
MIMO	Multi Input Multi Output
MPC	Model Predictive Control
MSE	Mean Square Error
PID	Proportional Integral Derivative
SMC	Sliding Mode Control
SISO	Single Input Single Output
SS	State-space
VSCS	Variable Structure Control Systems

CHAPTER 1
INTRODUCTION

1.1 Crane Systems

Cranes are one of the central equipments in industrial material handling as they play an important role in logistics and transportation. They are mainly used in intermediary roles in logistics processes, providing effective means to reorganize materials by lifting, transporting and stacking up. There are different types of cranes used throughout various industries. Main types are overhead, gantry, tower and boom cranes. Gantry cranes have integrated mechanical structure with rigid leg and wheels rolling on translation tracks, whereas overhead cranes translate on runway beams. Cranes are underactuated systems, therefore internal or external disturbances such as mechanical and electrical failures, high acceleration-deceleration rates, weather conditions and various unknown disturbances can decrease system stability resulting in abrupt motion during the transportation process, causing the load to swing, which in turn introduces serious problems such as mechanical wear, poor crane positioning capability, decreased productivity and even personnel injuries [17]. Many papers, introducing various open and closed loop control methods such as input shaping, command smoothing, fuzzy-logic, adaptive and robust control with different feedback elements such as vision feedback, inclinometer, accelerometer or encoder feedback are published to overcome this control problem [16].

Figure 1.1. Overhead crane

Figure 1.2. Gantry crane

Figure 1.3. Boom crane

The gantry crane is constructed of multiple parts. The bridge is the main and the heaviest structure that holds the payload. Trolley moves on the rails built on top of the bridge. The support legs hold the structure along with the saddle and side sills. The wheels enable the crane thus the payload to move along one axis, as the trolley allows payload to move along the perpendicular axis.

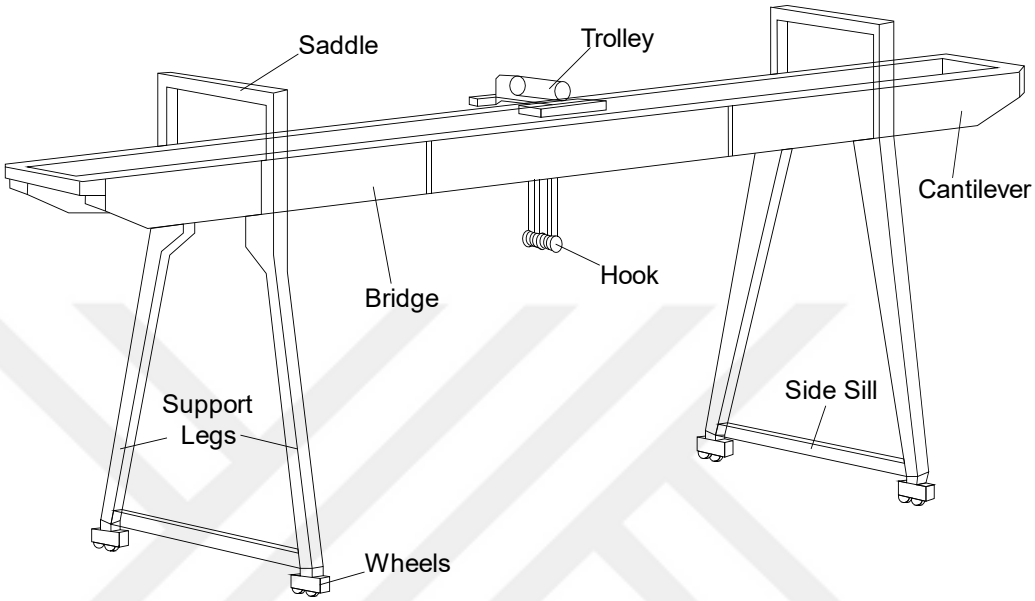

Figure 1.4. Structure drawing of gantry crane

1.2 Variable Structure Control Systems

Variable structure control systems (VSCS) are a class of robust control systems, which have roots in USSR as a result of the pioneering works of Emelyanov and Barbashin in the 1960s. Confined in USSR until the mid 1970s, this class of control systems were introduced to the world after the works by Itkis and Utkin, published in English. VSCS gained popularity and attention in short time, as it was applicable to robust controllers, state observers, model reference and adaptive controllers, tracking systems and many more with vast applicability to linear or nonlinear plants from aerodynamics, robotics, space systems to chemistry, industrial equipment subjects. [4]

VSCS encapsulates the control systems whereby the control law is changed according to the system states. In order to change the control law a definition for decision or boundary of change is necessary, which is called sliding surface. If the system states

exceed the boundary the control law switches back in order to retain the system states in the vicinity of the predefined sliding surface.

There are two main steps for designing the sliding controller, namely sliding surface design and control law design. The sliding surface is designed by transforming the equations into regular form and calculating the switching matrix with proper stability-based design approaches such as eigenvalue placement and quadratic minimization. The second step is to design the proper robust control law for the system dynamics and bounded uncertainties in order to compensate the partitioned system equations with control input resulting in system order reduction and disturbance rejection. The sliding or switching surface reflects one great advantage of sliding mode controller which is the order reduction, whereby the system dynamics reduces to the order of the sliding surface. If properly designed, complete system order collapse is even possible, which simplifies the overall control system and further enables cascaded sliding mode controller design topologies.

1.3 Literature Survey

There are various types of cranes with different control strategies. The overview for these systems were explained extensively in Ramli's paper [16] and in Abdelrahman's paper [17], whereby crane dynamics mathematical derivations for different types of cranes and various open and closed loop strategies for their control were introduced. Since the gantry or overhead crane consist of rigid bodies, it can be thought of a three dimensional pendulum system as derived and modelled in [20], [24] and [25]. The pure 3D pendulum nonlinear dynamics and its stabilization in the sense of Lyapunov are represented in the Chaturvedi's works [26] and [27] respectively. For operator in-loop scenarios open-loop command shaping control strategy is utilized, which is represented in Singhose's paper [19] as an overview for the span of 50 years. In [21] Raubar derives and compares open-loop ZV, ZVD, ZVDD shapers for the control of ship-to-shore cranes. Since cranes basically represent a 3D pendulum with different transporting mechanical structures, the difference between various types of cranes occurs mainly in the coordinate system representations of the payload position. Hence, resorting to works on different types of cranes proves to be useful, as Neupert in his paper [18] develops and demonstrates anti-sway and reference tracking for boom

cranes with proposed command shaping and MPC closed-loop control strategies with encoder and gyroscopes in the feedback loops. Kim [20] proposes state feedback control with integrator for setpoint tracking and sway velocity observer for gantry type container cranes and shows the results by applying the system to real cranes in the field. In [25], flatness-based state feedback with feedforward control is proposed and demonstrated for nonlinear overhead crane model. The thesis study [30] and paper [31] delve into the mechanical design of the complete gantry crane and overhead crane bridge respectively, which provide rich insight for the crane modelling. Golovin [22] and Tuan [23] consider the mechanical disturbance aspects of gantry and ship crane control, namely the vibrations in crane structure due to rigid body elasticity and actuator backlash. Golovin proposes H_∞ and Tuan proposes adaptive neural SMC robust controllers for the studied systems, simulating and testing them on laboratory cranes. The solutions used for the commercial crane control are demonstrated in Schneider Electric's whitepaper [28] and in Gustafsson's study in [29] with ABB. The references in [32], [33], [34], [35] and [36] are helpful for evaluating sliding mode control for different systems with various dynamic models.

1.4 Motivation of Study

In this study, the gantry crane system responses to the LQR, PID and SMC controllers are derived, simulated and compared. Since mostly the state feedback and PID control strategies are utilized in the industrial area, a proper comparison with a novel robust control strategy like SMC should demonstrate the advantages of controller improvement for the aforementioned systems.

CHAPTER 2
THEORETICAL BACKGROUND

2.1 System Dynamic Modelling

Systems can be mathematically modelled in various ways. The traditional ways of modelling are the Newtonian and the more recent Lagrangian approaches. In the Newtonian approach, the system dynamics is solved by considering all of the acting forces on free bodies in a system. Each free body is thought to be independent, by reflecting all other forces that are acting on it. Thus, the modelling of the overall system is achieved by closing the force "loops" by considering each free body separately, which gives result to the motion of equations of the system. Since the forces act on free bodies according to the system constraints, the resulting system motion equations include constraints of the system naturally. Newtonian approach of constructing force vector according to the constraints complicates the calculations. In the Lagrangian approach, however, the directions of forces do not matter, since the system dynamics is solved based on the energy formulas and the constraints are enforced on the very beginning when selecting the generalized coordinates. The Lagrangian formula [6], [13]

$$L = T - V \tag{2.1}$$

where the scalars T and V are the kinetic and the potential energy of the free bodies, represents the difference between the energies of a free body. Since only the rigid bodies are considered here, free body can be thought as a particle with point mass. If particle's total path $x_0(t)$ yields a local minima, local maxima or local saddle point from the principle of stationary action functional within a definite time interval

$$S = \int_{t_1}^{t_2} L(x, \dot{x}, t)dt \tag{2.2}$$

and its motion equations reduce to the Euler-Lagrange equations below, assuming the system constraints are holonomic and free bodies are rigid [5]

$$\frac{d}{dt}\left(\frac{\partial L}{\partial \dot{q}_j}\right) - \frac{\partial L}{\partial q_j} = Q_j \tag{2.3}$$

where the term q_j represents the generalized coordinates and Q_j represents the virtual work done due to the external forces that act upon free bodies. The generalized coordinates q_j usually, but not necessarily, represent the minimum number of coordinates that the motion of a free body can be expressed. Hence, the most common coordinate systems are not enforced on the studied system, rendering the modelling approach more flexible. The virtual work or generalized force is defined as

$$Q_j = \sum_i F_i . \delta r_i = \sum_i F_i \frac{\partial r_i}{\partial q_j} \tag{2.4}$$

where δr_i is the virtual displacement of the particle and the force F_i usually represents the nonconservative forces. [6]

Calculating the Euler-Lagrange equations reveals the motions of equations of a system, by imposing the constraints at the very beginning of the calculation when forming the system's path equations. This greatly eases and accelerates the calculation steps by reducing the number of unknown variables in a system. Here, the constraints dealt with are assumed to be positional constraints or holonomic constraints as they are called, meaning that the number of generalized coordinates is equal to the number of degrees of freedom of the system, which is revealed by expressing the positional relationship of particles by exact equalities. The revealed equations of motion can be nonlinear depending on the system's nature. In order to linearize the nonlinear equations of motion second order Taylor expansion around the expansion point a can be applied, thus small variation approximation in system coordinates is achieved. As a result, the linearized system possesses similar characteristics as the nonlinear system around the expansion point.

$$f(x) = \sum_{n=0}^{\infty} \frac{f^{(n)}(a)}{n!}(x-a)^n \tag{2.5}$$

2.2 Control System Design

2.2.1 LQR Controller Design

Consider the linear state-space representation of a plant below

$$\begin{cases} \dot{x} = Ax + Bu \\ y = Cx + Du \end{cases} \tag{2.6}$$

with $A \in R^{nxn}$, $B \in R^{nxm}$, B is full rank having linearly independent column vectors, indicating that every control signal's action on the system is linearly independent and $1 \leq m \leq n$. The system (2.6) can be controlled by LQR pole placement, if it is completely state controllable. The state feedback control law is defined by $u = -Kx$, where K is called the state feedback gain matrix. The controllability matrix C_{ctrl}

$$C_{ctrl} = [B \quad AB \quad \dots \quad A^{n-1}B] \tag{2.7}$$

must have full rank for arbitrary pole placement, meaning that the system is completely controllable. In order to determine the state feedback matrix by LQR the performance index J below is kept at a minimum.

$$J = \int_0^\infty (x^T Q x + u^T R u) dt \tag{2.8}$$

Here, Q and R are both positive definite and symmetric matrices. Q represents the cost matrix for state errors and R represents the penalty for controller effort. Solving the corresponding reduced-matrix Riccati equation in (2.9) gives the solution for this performance index, by which we can further calculate the feedback gain matrix K. [1]

$$A^T P + PA - PBR^{-1}B^T P + Q = 0 \tag{2.9}$$

The matrix P is the solution of this Riccati equation and the gain matrix is calculated as in the following equation.

$$K = R^{-1}B^T S \tag{2.10}$$

2.2.2 PID Controller Design

PID controllers are central to most industrial controllers used in the field today. The generic PID controller with setpoint weighting feedforward and derivative filtering mechanism is introduced below [2]:

$$F(s) = \frac{K_p b + \frac{K_i}{s} + K_d c \frac{Ns}{s+N}}{K_p + \frac{K_i}{s} + K_d \frac{Ns}{s+N}} \tag{2.11}$$

$$C(s) = K_p + \frac{K_i}{s} + K_d \frac{Ns}{s+N} \tag{2.12}$$

$F(s)$ represents the feedforward term with setpoint weighting and $C(s)$ is the PID controller with derivative filtering. The figure below represents the block diagram of the PID control system. The term $G_p(s)$ is the plant transfer function. [8]

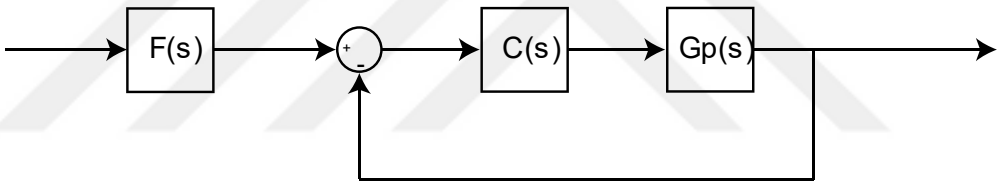

Figure 2.1. PID control system block diagram

There are various approaches for tuning the PID controllers, namely the experimental Ziegler-Nichols tuning method, frequency-response method and computational optimization method. For complex plants the tuning for PID is mostly done on site experimentally, since the plant model cannot be obtained due to its complexity. For such plants Ziegler-Nichols method of tuning is exceptionally important. If the plant's mathematical model is available, other methods of tuning can be utilized to calculate and simulate the system's response to PID control action for determining the gain values.

2.2.3 SMC Controller Design

The subsequent sliding mode design steps are mostly referenced from [3], [12] and [14].

Designing the sliding mode controller mainly consists of two steps: sliding surface design and control law design. Considering the LTI state-space system in equation (2.6), the linear switching function is defined as the linear combination of the states:

$$\sigma(x) = Sx(t) \tag{2.13}$$

where $t, x \in R^n$. The hyperplane S_p, on which the sliding motion takes place, is designed to be the null space of the switching matrix S.

$$S_p: \sigma(x) = Sx(t) = 0 \tag{2.14}$$

The sliding motion of the system evolves into two phases as the control action is active: reaching phase and sliding phase. If properly designed, after the reaching phase as $t \geq t_r$ the control signal frequency becomes ideally infinite, locking the system to the sliding surface during the sliding phase.

The derivative of the switching function can be combined with the state-space representation in the equation (2.6) as

$$\dot{\sigma}(x) = S\dot{x}(t) = SAx + SBu = 0 \tag{2.15}$$

thus, the equivalent control is derived as

$$u_{eq}(t) = -(SB)^{-1}SAx(t) \tag{2.16}$$

The matrix SB in the equation above is designed to be non-singular with the proper choice of matrix S. The equivalent control represents the required control action to ensure the imminent start of the sliding phase right from near the beginning by compensating the system dynamics. If the equivalent control is substituted for the control signal u in the original system equation in (2.6), the resulting equation represents the motion of the states in the sliding phase.

$$\dot{x(t)} = (I_n - B(SB)^{-1}S)Ax(t) = (I_n - I_n)Ax(t) = 0 \tag{2.17}$$

If an additional matched uncertainty term is added to the input channel, the state-space equation in (2.6) becomes

$$\dot{x(t)} = Ax(t) + B\big(u(t) + \xi(t,x)\big) \tag{2.18}$$

The corresponding equivalent control becomes

$$u_{eq}(t) = -(SB)^{-1}SAx(t) - \xi(t,x) \tag{2.19}$$

The equivalent control in the equation above is not directly realizable, since the exact nature of the uncertainty is unknown in most cases. Instead, information about the upper bound for the absolute value of the uncertainty enables its compensation with the help of the sliding mode switching function. The proposed control action for this perturbed system

$$u(t) = -(SB)^{-1}SAx(t) - (\eta_0 + \eta_1(t,x)|SB|)(SB)^{-1}sign\big(\sigma(t)\big) \tag{2.20}$$

reduces the switching variable's, therefore the system's equation to

$$\dot{\sigma}(x) = SB\xi(t,x) - \eta_0 sign\big(\sigma(t)\big) - \eta_1(t,x)|SB|sign\big(\sigma(t)\big) \tag{2.21}$$

Where η_0 represents the control gain affecting the reaching time interval and η_1 is the upper bound for the uncertainty, so that $|\xi(t,x)| \leq \eta_1$. If the properly designed third term in (2.21) compensates the first term of uncertainty, hence the system equation reduces further to

$$\dot{\sigma}(x) = -\eta_0 sign\big(\sigma(t)\big) \tag{2.22}$$

which shows the chattering effect in the controlled system states due to the switching function and the matched uncertainty ξ in the control input path is completely rejected.

In order to study the system's stability under the control action without solving the system's equation, a proper Lyapunov candidate function is introduced as follows

$$V = \frac{1}{2}\sigma(t)^2 \geq 0 \tag{2.23}$$

and its derivative

$$\begin{aligned}\dot{V} = \sigma(t)\dot{\sigma}(t) &= SB\sigma(t)\xi(t,x) - \eta\sigma(t)sign\big(\sigma(t)\big) - \eta_1(t,x)|SB|\sigma(t)sign\big(\sigma(t)\big) \\ &\leq |SB||\sigma(t)|\eta_1(t,x) - \eta|\sigma(t)| - \eta_1(t,x)|SB||\sigma(t)| \\ &= -\eta_0|\sigma(t)| < 0\end{aligned} \tag{2.24}$$

with the matrix SB is non-singular. In order to verify the stability condition, the candidate function and its derivate should have opposite signs. This means if the candidate function is positive definite, its derivative should be negative definite and vice versa. This condition is attested in the equations (2.23) and (2.24) above, proving that the sliding variable's reaching time to 0 is finite.

In order to design the switching matrix, LTI system equations in (2.6) are transformed into the regular form by orthogonal transformation matrix T, which is not unique and determined by QR factorization with upper triangular matrix R. The following transformations are applied [9]:

$$T\dot{x} = TAT^TTx + TBu \tag{2.25}$$

Since the transformation matrix T is orthogonal, its transpose is equal to its inverse. The resulting regular system has the following representation:

$$\begin{bmatrix}\dot{z_1}\\ \dot{z_2}\end{bmatrix} = \begin{bmatrix}A_{11} & A_{12}\\ A_{21} & A_{22}\end{bmatrix}\begin{bmatrix}z_1\\ z_2\end{bmatrix} + \begin{bmatrix}0\\ B_2\end{bmatrix}u \tag{2.26}$$

whereas z_1 represents the virtual system states with $z_1 \in R^{n-m}$ and z_2 represents the virtual control with $z_2 \in R^m$. The same transformation is also applied to the sliding surface:

$$\sigma = ST^TTx = S_Tz = [S_1\ S_2]\begin{bmatrix}z_1\\ z_2\end{bmatrix} \tag{2.27}$$

During the sliding motion the sliding variable equation becomes

$$\sigma(t) = S_Tz(t) = 0 \tag{2.28}$$

Substituting the equation above to the transformed system equation in (2.26) results in the switching matrix

$$S = S_TT = S_2[S_2^{-1}S_1\ I_m]T = S_2[M\ I_m]T \tag{2.29}$$

There are various methods to use for determining the switching matrix. Eigenvalue placement can either be made by intelligent selection of the characteristic equation roots or by determining them with quadratic minimization. In this study, in order to design the switching matrix, the second method, namely LQR, will be used, since it also inherits conditional robustness for the unmatched uncertainty in the plant characteristic equation. In order to design with LQR, the performance index in (2.30) is to be kept at minimum.

$$J = \frac{1}{2}\int_{t_r}^{\infty} x^T Q x dt \tag{2.30}$$

After the orthogonal transformation the quadratic performance index function becomes

$$J = \frac{1}{2}\int_{t_r}^{\infty} \left(z_1^T \hat{Q} z_1 + v^T Q_{22} v\right) dt \tag{2.31}$$

whereby the new cost matrix for the transformed states is equal to

$$\hat{Q} = Q_{11} - Q_{12} Q_{22}^{-1} Q_{12}^T \tag{2.32}$$

and the new virtual control is equal to

$$v = z_2 + Q_{22}^{-1} Q_{12}^T z_1 \tag{2.33}$$

Thus, the transformed system equation becomes

$$\dot{z_1} = (A_{11} - A_{12} Q_{22}^{-1} Q_{12}^T) z_1 + A_{12} v = \hat{A} z_1 + A_{12} v \tag{2.34}$$

with

$$\hat{A} = (A_{11} - A_{12} Q_{22}^{-1} Q_{12}^T) \tag{2.35}$$

Solving the corresponding Riccati matrix equation

$$\hat{A}^T \hat{P} + \hat{P}\hat{A} - \hat{P} B R^{-1} B^T \hat{P} + \hat{Q} = 0 \tag{2.36}$$

gives the solution for this performance index, by which the sliding surface coefficients can further be calculated. The resulting surface parametrizing matrix in (2.29) is

$$M = Q_{22}^{-1} Q_{12}^{T} + Q_{22}^{-1} A_{12}^{T} \hat{P} \tag{2.37}$$

whereby $\hat{P}$ is the solution to the Riccati equation. Finally, the sliding surface matrix S can be calculated with

$$S = S_2 [M \; I_m] T \tag{2.38}$$

As previously stated, since the resulting switching matrix S is designed with LQR, it also inherits robustness against the unmatched uncertainty in the plant dynamics.

CHAPTER 3
PRACTICAL IMPLICATIONS

3.1 Crane Mathematical Modelling

There are various types of cranes as introduced in the first chapter. In this study, the main focus is on gantry type cranes which are actually very similar to overhead cranes except the rigid legs with wheels. Gantry crane consists of bridge structure for holding the payload, legs with wheels for translation of the bridge along the horizontal axis. For the other direction of horizontal axis, trolley is used for translation, which has significantly lower weight compared to the bridge and trolley together. Therefore, the payload swing trajectory varies according to the translation axis, which can be calculated with different weights iteratively, as the same motion of equations are used for both dimensions and only the weight values change.

In this study, the gantry crane is treated as a rigid body, so that its whole weight is thought to be concentrated in a point mass, which is equal to addition of both bridge mass m_b and trolley mass m_t along the x-axis and only to the trolley mass m_t along the y-axis. Payload is hung to the trolley with an ideal nonelastic rope of infinitesimal thickness and length l. Payload and hook are considered as a single point of mass m_p at the opposite end of the rope.

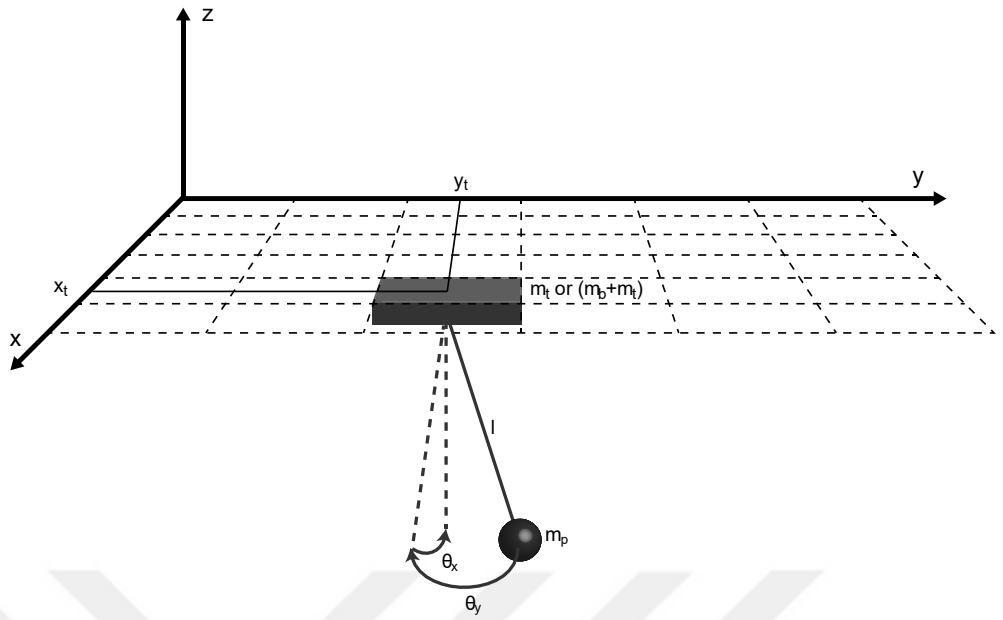

Figure 3.1. Drawing of the simplified crane model

Firstly, the trolley and payload position vectors in cartesian coordinates are determined. Trolley position vector is $x_t, y_t \in R^n$ and $z_t = 0$. Payload position coordinates are defined as below. [7]

$$\begin{cases} x_p = x_t + l\sin(\theta_x) \\ y_p = y_t + l\cos(\theta_x)\sin(\theta_y) \\ z_p = -l\cos(\theta_x)\cos(\theta_y) \end{cases} \tag{3.1}$$

In the Lagrangian equation in (2.1) the kinetic energy T and the potential energy V of the rigid bodies are defined as $T = \frac{1}{2}(m_b + m_t)v_x^2 + \frac{1}{2}m_t v_y^2 + \frac{1}{2}m_p v_p^2$ and $V = m_p g z_p$ [10], whereby m_t, m_p, v_t, v_p are trolley and payload mass and velocities, z_p is the payload vertical z-axis position. The velocities are derived by taking the derivative of the position vectors.

$$L = T - V = \frac{1}{2}(m_b + m_t)v_x^2 + \frac{1}{2}m_t v_y^2 + \frac{1}{2}m_p v_p^2 - m_p g z_p \tag{3.2}$$

Q_j in Euler-Lagrange equation in (2.3) represents the virtual work due to the external forces that act upon the crane bodies. Force that drives the trolley to the required

position, friction force on the rail tracks and gears, wind resistance on the payload are such forces. Since the ideal system is considered, only the trolley driving force is included in the equation below. The friction forces are omitted. The paper in [15] is suggested to be studied in order to gain insight into the nature of friction and to include such forces in the formula.

$$\frac{d}{dt}\left(\frac{\partial L}{\partial \dot{q}_j}\right) - \frac{\partial L}{\partial q_j} = F \tag{3.3}$$

The Euler-Lagrange equation is solved with respect to the crane trolley and payload kinetic and potential energy for each crane generalized coordinate, namely x_t, y_t, l, θ_x, θ_y. The resulting equations are nonlinear and very long to include in this paper. Instead, second order Taylor series expansion around 0° angle is calculated, which yields the small angle approximation. The change in rope length during the crane movement is also assumed to be 0, therefore $\dot{l} = 0$ and $\ddot{l} = 0$, which is thought to be adjusted before the movement. The viscous friction coefficient k along the x and y axes is also assumed to be 0. The resulting linearized crane mathematical dynamic equations are:

$$\begin{cases} q_{x_t}: (m_b + m_t + m_p)\ddot{x}_t - F_x + m_p l\ddot{\theta}_x = 0 \\ q_{y_t}: (m_t + m_p)\ddot{y}_t - F_y + m_p l\ddot{\theta}_y = 0 \\ q_l: m_p(\theta_x \ddot{x}_t - g + \theta_y \ddot{y}_t) = 0 \\ q_{\theta_x}: m_p l(l\ddot{\theta}_x + g\theta_x + \ddot{x}_t) = 0 \\ q_{\theta_y}: m_p l(l\ddot{\theta}_y + g\theta_y + \ddot{y}_t) = 0 \end{cases} \tag{3.4}$$

There are five equations in (3.4), each corresponding to one generalized coordinate, namely x_t, y_t, l, θ_x, θ_y. Being decoupled in the linearized model in contrast to the original nonlinear model, the first two equations represent the movement along the cartesian coordinates. The third equation couples the x and y coordinates for the payload. The last two equations together with the first two equations yield the angle of the rope and position of the trolley along the x and y axes.

In order to isolate the positional and angular accelerations, the equations in (3.4) were solved together, yielding the equations of motion along the generalized coordinates below.

$$\begin{cases} \ddot{x_t} = \dfrac{m_p}{(m_b + m_t)} g\theta_x + \dfrac{1}{(m_b + m_t)} F_x \\ \ddot{\theta_x} = -\dfrac{m_p + (m_b + m_t)}{(m_b + m_t)} \dfrac{g}{l} - \dfrac{1}{(m_b + m_t) l} F_x \\ \ddot{y_t} = \dfrac{m_p}{m_t} g\theta_y + \dfrac{1}{m_t} F_y \\ \ddot{\theta_y} = -\dfrac{m_p + m_t}{m_t} \dfrac{g}{l} - \dfrac{1}{m_t l} F_y \end{cases} \tag{3.5}$$

After applying the second order Taylor expansion the equations of motion along the x and y axes become decoupled and symmetric in structure, giving the possibility for use of two decoupled identical controllers by treating each axis separately. The only difference between axes stems from the fact that both bridge and trolley weights move while the crane translates along the x-axis and only the trolley moves along the y-axis.

The trajectory plots for trolley, payload and rope as positional snapshots resulting from direct crane positioning trajectory $x_t(t) = t$ along the x-axis and $y_t(t) = t(1 + \sin t)$ along the y-axis is presented in **Figure 3.2** for inspection. Since the position trajectory was directly input to the system, the driving forces along the both x and y axes were held at 0. The simulation values for crane dynamics variables are selected as below.

Table 3.1. Crane mathematical model variables

Variable	Explanation	Value
l	Rope length	10 m
m_b	Bridge mass	200 t
m_t	Trolley mass	40 t
m_p	Payload mass	16 t

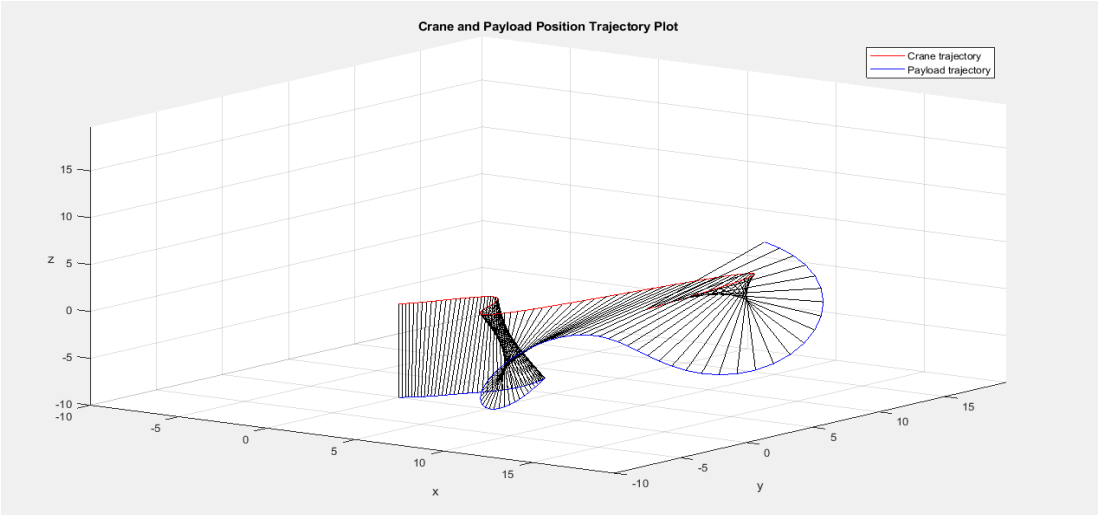

Figure 3.2. Crane and payload position trajectory plot.

The red line in **Figure 3.2** represents crane trolley, blue line represents payload and black lines represent the rope at periodic time intervals.

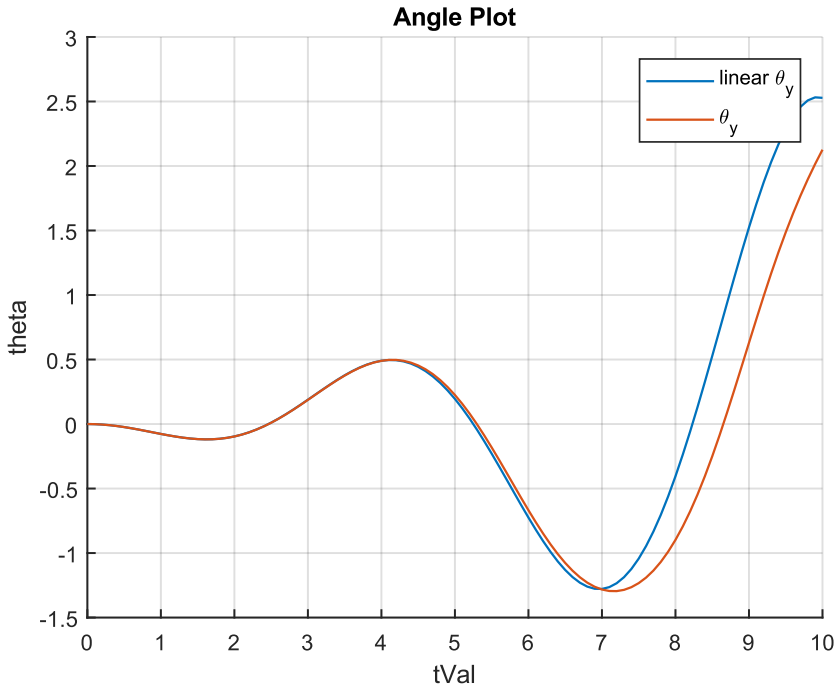

Figure 3.3. Linear versus nonlinear payload angle plot

In **Figure 3.3** the plot of the linear and nonlinear angles resulting from direct positioning trajectories is shown. The y-axis angle of the linearized model deviates

from the nonlinear original model as it becomes much larger than 0. The angle is only affected from the acceleration along the same axis, the x-axis trajectory has no impact on the angle θ_x, because it has a constant velocity.

3.2 Crane Control System Design

The state-space equation derived from the linearized crane model for x-axis is stated below. Since both x and y axes are decoupled in the linearized equations, the y-axis state-space equation happens to be exactly the same structure, which means two identical controllers can run independently in parallel for each axis for the same crane. The only difference between the two axes lies in the different total of weights that move along them.

$$\begin{bmatrix} \dot{x}_t \\ \ddot{x}_t \\ \dot{\theta}_x \\ \ddot{\theta}_x \end{bmatrix} = \begin{bmatrix} 0 & 1 & 0 & 0 \\ 0 & 0 & \frac{m_p}{m_b + m_t} g & 0 \\ 0 & 0 & 0 & 1 \\ 0 & 0 & -\frac{m_p + m_b + m_t}{m_b + m_t} \frac{g}{l} & 0 \end{bmatrix} \begin{bmatrix} x_t \\ \dot{x}_t \\ \theta_x \\ \dot{\theta}_x \end{bmatrix} + \begin{bmatrix} 0 \\ \frac{1}{m_b + m_t} \\ 0 \\ -\frac{1}{(m_b + m_t) l} \end{bmatrix} u_x \tag{3.6}$$

The control input u_x represents the crane driving force F_x in units of Newton [N] along the x-axis. Similarly, the state-space equation for y-axis is stated below.

$$\begin{bmatrix} \dot{y}_t \\ \ddot{y}_t \\ \dot{\theta}_y \\ \ddot{\theta}_y \end{bmatrix} = \begin{bmatrix} 0 & 1 & 0 & 0 \\ 0 & 0 & \frac{m_p}{m_t} g & 0 \\ 0 & 0 & 0 & 1 \\ 0 & 0 & -\frac{m_p + m_t}{m_t} \frac{g}{l} & 0 \end{bmatrix} \begin{bmatrix} y_t \\ \dot{y}_t \\ \theta_y \\ \dot{\theta}_y \end{bmatrix} + \begin{bmatrix} 0 \\ \frac{1}{m_t} \\ 0 \\ -\frac{1}{m_t l} \end{bmatrix} u_y \tag{3.7}$$

The Laplace s-domain block diagram representation derived from the equations in (3.5) for one axis is shown in the figure below. The symbol x in the block diagram indicates the position. Expanded block diagram is especially helpful and suitable for individual signal tracing. [11]

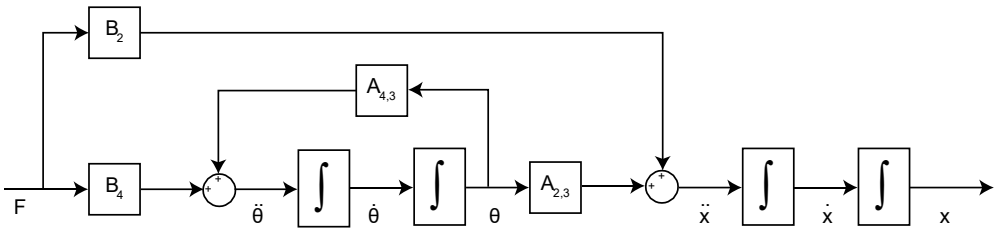

Figure 3.4. Crane model transfer function block diagram for one axis

Three types of controllers are designed for the control of the crane dynamics: LQR state feedback controller, PID controller with LQR and SMC with LQR.

3.2.1 LQR State Feedback Controller Design

The crane has different weight along the x and y axes. Along the x-axis both the bridge and trolley translates, whereas along the y-axis only the trolley translates. The crane model along the bridge translating x-axis with respect to the selected variable values as indicated in **Table 3.1** results in the following system state-space equation.

$$\begin{bmatrix} \dot{x}_t \\ \ddot{x}_t \\ \dot{\theta}_x \\ \ddot{\theta}_x \end{bmatrix} = \begin{bmatrix} 0 & 1.0000 & 0 & 0 \\ 0 & 0 & 0.6540 & 0 \\ 0 & 0 & 0 & 1.0000 \\ 0 & 0 & -1.0464 & 0 \end{bmatrix} \begin{bmatrix} x_t \\ \dot{x}_t \\ \theta_x \\ \dot{\theta}_x \end{bmatrix} + \begin{bmatrix} 0 \\ 0.4167 \times 10^{-5} \\ 0 \\ -0.0416 \times 10^{-5} \end{bmatrix} u \qquad (3.8)$$

Similarly, the crane state-space equation along the trolley translating y-axis is as below:

$$\begin{bmatrix} \dot{y}_t \\ \ddot{y}_t \\ \dot{\theta}_y \\ \ddot{\theta}_y \end{bmatrix} = \begin{bmatrix} 0 & 1.0000 & 0 & 0 \\ 0 & 0 & 3.9240 & 0 \\ 0 & 0 & 0 & 1.0000 \\ 0 & 0 & -1.3734 & 0 \end{bmatrix} \begin{bmatrix} y_t \\ \dot{y}_t \\ \theta_y \\ \dot{\theta}_y \end{bmatrix} + \begin{bmatrix} 0 \\ 0.2500 \times 10^{-4} \\ 0 \\ -0.0250 \times 10^{-4} \end{bmatrix} u \qquad (3.9)$$

Checking the rank of controllability matrix C of the LTI crane system above is necessary in order to assure full state arbitrary pole placement. The controllability matrix for x-axis model is

$$C_x = \begin{bmatrix} 0 & 0.4167 & 0 & -0.0392 \\ 0.5 & 0 & -0.0392 & 0 \\ 0 & -0.05 & 0 & 0.0530 \\ -0.05 & 0 & 0.0530 & 0 \end{bmatrix} \times 10^{-5} \tag{3.10}$$

for the y-axis

$$C_y = \begin{bmatrix} 0 & 0.2500 & 0 & -0.0981 \\ 0.2500 & 0 & -0.0981 & 0 \\ 0 & -0.0250 & 0 & 0.0343 \\ -0.0250 & 0 & 0.0343 & 0 \end{bmatrix} \times 10^{-4} \tag{3.11}$$

Both have a rank of 4, which indicates the system is controllable. In order to calculate the state feedback matrix by LQR the performance index J in equation (2.8) should be as small as possible. This is achieved by solving the corresponding Riccati equation with respect to the selected state cost matrix Q and control action cost matrix R for the x-axis indicated below.

$$Q_x = \begin{bmatrix} 5 \times 10^8 & 0 & 0 & 0 \\ 0 & 1 \times 10^2 & 0 & 0 \\ 0 & 0 & 5 \times 10^{11} & 0 \\ 0 & 0 & 0 & 1 \times 10^2 \end{bmatrix} \tag{3.12}$$

$$R_x = 0.1$$

Although normally, the cost matrices should be designed separately for both x and y axes since their dynamics are different, the same cost matrix will be used for both axes for robustness comparison purposes under system matrix changes, as the cost matrices for the LQR-PID and LQR-SMC controllers will also be not changed in the next sections.

$$Q_y = \begin{bmatrix} 5 \times 10^8 & 0 & 0 & 0 \\ 0 & 1 \times 10^2 & 0 & 0 \\ 0 & 0 & 5 \times 10^{11} & 0 \\ 0 & 0 & 0 & 1 \times 10^2 \end{bmatrix} \tag{3.13}$$

$$R_y = 0.1$$

According to the cost functions above the emphasis is on the position and angle errors. Finding the solution $\hat{P}$ for the Riccati equation in (2.9) and substituting into (2.10) results in the following gain matrices:

$$K = [0.0707 \quad 0.2509 \quad -1.8549 \quad -0.9979] \times 10^6 \tag{3.14}$$

The LQR control system block diagram is shown in the figure below.

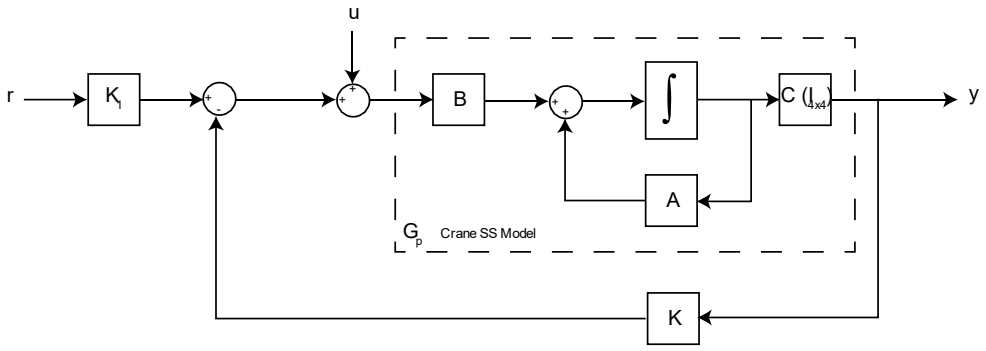

Figure 3.5. LQR control overall system block diagram

3.2.2 LQR-PID Controller Design

In the previous section the state feedback gain matrix provides basic close loop performance for proper reference tracking and state control. In the presence of disturbances, the LQR control method falls short of stabilizing the system without causing high deviations from the reference value. Hence, the addition of cascaded PID controllers for each state will meet the need for system's accuracy and robustness.

Since all of the four states are controlled with four cascaded PID controllers, overall system complexity increases beyond a proper computational optimization. Therefore, the PID parameters were adjusted by educated guess with many iterations of simulation. Since the selected PID parameters give satisfactory performance for both x and y motion axes the same parameters are used for controlling them. The attained PID parameters with satisfactory crane model control are indicated in the table below.

Table 3.2. PID controller parameters

State Name	Controller	K_p	K_i	K_d	N	P_w	D_w	EnI

x1 Position	PIDx1	1.2	0.3	0	20	1	1	20
x2 Velocity	PIDx2	1.5	0.5	0	20	1	1	50
x3 Angle	PIDx3	2.0	0.2	0.1	20	1	1	100
x4 Angular Velocity	PIDx4	1.5	0	0	20	1	1	100

The inner block diagram of the PID controller is shown in **Figure 3.6** below. For increased stability, the integrator term is designed to be adaptive to the error margin so that it is activated by a user-defined percentage of reference deviation. For example, if the EnI parameter is set to 20%, the integrator starts to integrate with a gain of 0% as the PID feedback is in the 20% vicinity of the reference value. Thus, the integration overshoot is prevented due to large PID errors as the reference value changes. As the feedback approaches the reference value the integration gain increases up to 100% having full activation.

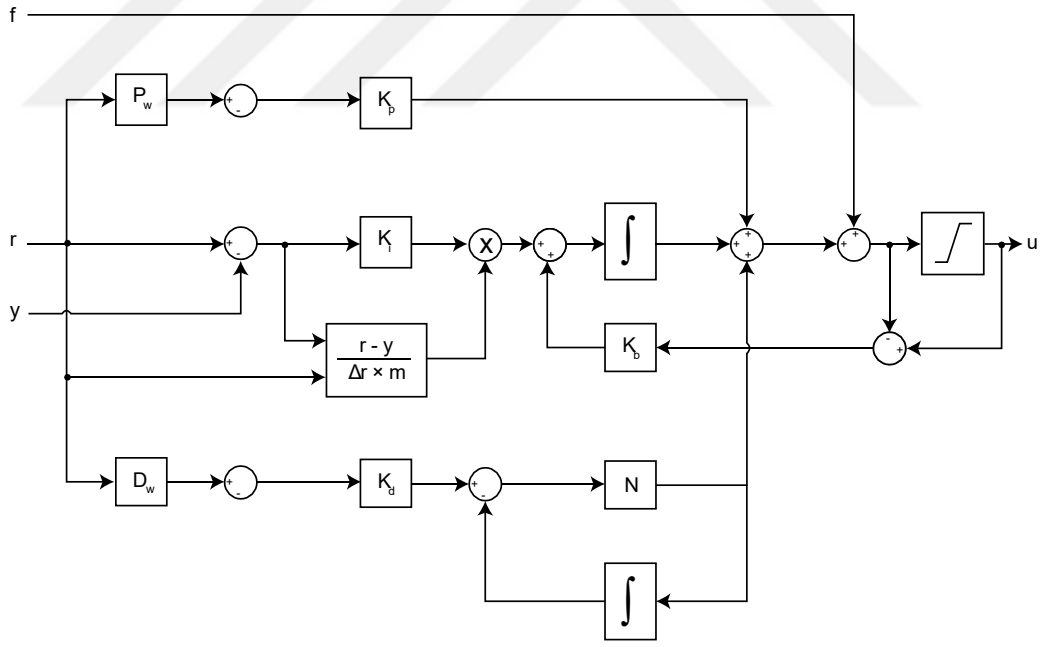

Figure 3.6. PID controller subsystem block diagram

The LQR-PID control overall system block diagram is shown in the figure below.

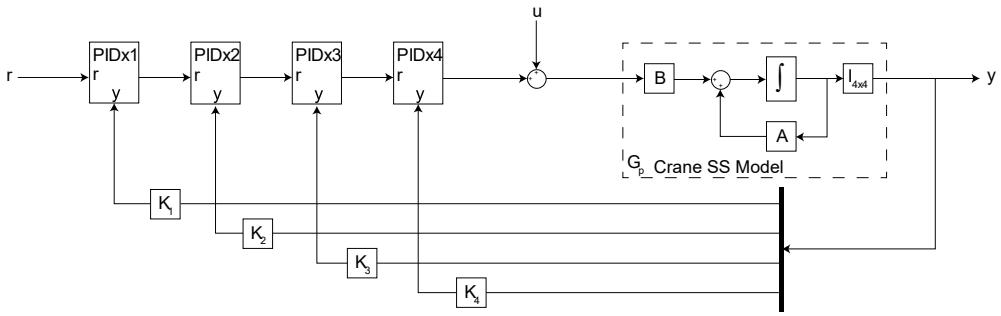

Figure 3.7. LQR-PID control overall system block diagram

3.2.3 LQR-SMC Controller Design

As indicated in the section 2.2.3 the control law is determined as follows:

$$u(t) = -(SB)^{-1}SAx(t) - (\eta_0 + \eta_1(t,x)|SB|)(SB)^{-1}sign\big(\sigma(t)\big) \qquad (3.15)$$

In order to design the switching matrix with ease, the crane state-space model in equation (3.6) should be transformed into the regular form by coordinate transformation matrix T, which is calculated by Matlab's QR factorization command qr. Since in Matlab the solution yields an upper triangular matrix R with the corresponding orthogonal matrix, the rows of matrices were manipulated simultaneously by swapping rows to obtain the appropriate lower triangular matrix R and the corresponding orthogonal transformation matrix T. The resulting matrices are indicated in equation (3.16) below.

$$T = \begin{bmatrix} 0.0995 & 0.0990 & 0 & 0.9901 \\ 0 & 0 & 1.0000 & 0 \\ -0.9950 & 0.0099 & 0 & 0.0990 \\ 0 & -0.9950 & 0 & 0.0995 \end{bmatrix}$$
$$R = \begin{bmatrix} 0 \\ 0 \\ 0 \\ -0.5025 \end{bmatrix} \times 10^{-5} \qquad (3.16)$$

After applying the transformation to the system matrices, the result yields crane state-space model partitioned in the regular form as indicated in (2.26).

$$\begin{bmatrix} \dot{z_1} \\ \dot{z_2} \end{bmatrix} = \begin{bmatrix} A_{11} & A_{12} \\ A_{21} & A_{22} \end{bmatrix} \begin{bmatrix} z_1 \\ z_2 \end{bmatrix} + \begin{bmatrix} 0 \\ B_2 \end{bmatrix} u \tag{3.17}$$

where the corresponding system and input matrices are

$$\begin{aligned} A_{11} &= \begin{bmatrix} 0.0099 & -0.9713 & 0.0010 \\ 0.9901 & 0 & 0.0990 \\ -0.0985 & -0.0971 & -0.0099 \end{bmatrix} \\ A_{12} &= \begin{bmatrix} -0.0990 \\ 0.0995 \\ 0.9901 \end{bmatrix} \\ A_{21} &= \begin{bmatrix} 0 & -0.8863 & 0 \end{bmatrix} \\ A_{22} &= 0 \end{aligned} \tag{3.18}$$

$$\begin{aligned} B_1 &= \begin{bmatrix} 0 \\ 0 \\ 0 \end{bmatrix} \\ B_2 &= -5.0249 \times 10^{-6} \end{aligned} \tag{3.19}$$

In order to design the switching surface with LQR, the modified quadratic minimization function in (3.20) should be solved for its corresponding Riccati equation as indicated in equation (2.36).

$$J = \frac{1}{2} \int_{t_r}^{\infty} \left(z_1^T \hat{Q} z_1 + v^T Q_{22} v \right) dt \tag{3.20}$$

The state cost matrix Q is selected as follows:

$$Q = \begin{bmatrix} 2 \times 10^3 & 0 & 0 & 0 \\ 0 & 1 \times 10^4 & 0 & 0 \\ 0 & 0 & 2 \times 10^6 & 0 \\ 0 & 0 & 0 & 2 \times 10^6 \end{bmatrix} \tag{3.21}$$

The transformation matrix T is applied to the state cost matrix Q in order to get the transformed matrix Q_T as shown below:

$$Q_T = \begin{bmatrix} 1.9607 & 0 & 0.1959 & 0.1961 \\ 0 & 2.0000 & 0 & 0 \\ 0.1959 & 0 & 0.0216 & 0.0196 \\ 0.1961 & 0 & 0.0196 & 0.0297 \end{bmatrix} \times 10^6 \tag{3.22}$$

The submatrices of Q_T are

$$Q_{T_{11}} = \begin{bmatrix} 1.9607 & 0 & 0.1959 \\ 0 & 2.0000 & 0 \\ 0.1959 & 0 & 0.0216 \end{bmatrix} \times 10^6$$

$$Q_{T_{12}} = \begin{bmatrix} 1.9605 \\ 0 \\ 0.1961 \end{bmatrix} \times 10^5 \tag{3.23}$$

$$Q_{T_{21}} = [1.9605 \quad 0 \quad 0.1961] \times 10^5$$

$$Q_{T_{22}} = 2.9703 \times 10^4$$

The new transformed cost matrix $\hat{Q}$ as indicated in (2.32) is

$$\hat{Q} = \begin{bmatrix} 0.6667 & 0 & 0.0665 \\ 0 & 2.0000 & 0 \\ 0.0665 & 0 & 0.0086 \end{bmatrix} \times 10^6 \tag{3.24}$$

and the new system matrix $\hat{A}$ defined in (2.35) is

$$\hat{A} = \begin{bmatrix} 0.6634 & -0.9713 & 0.0663 \\ 0.3333 & 0 & 0.0333 \\ -6.6336 & -0.0971 & -0.6634 \end{bmatrix} \tag{3.25}$$

Calculating the Riccati equation with respect to the transformed new matrices gives solution for the sliding surface parameterizing matrix M:

$$M = [0.1909 \quad 11.5451 \quad 0.2799] \tag{3.26}$$

Finally, the switching matrix is calculated as in the equation (2.38) as follows:

$$S = [-0.2595 \quad -0.9734 \quad 11.5451 \quad 0.3163] \tag{3.27}$$

The LQR-SMC block diagram implementing the switching control according to the sliding surface is shown in the figure below.

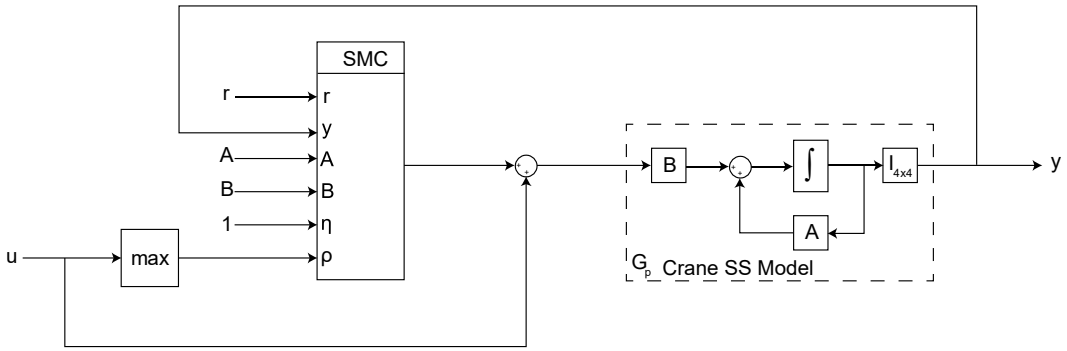

Figure 3.8. LQR-SMC control overall system block diagram

3.3 Notes on Implementation and Instrumentation

The material so far presented was the theoretical foundation for gantry crane control. When properly implemented to real world systems, theoretical aspects come into prominence. For real gantry cranes in the logistics field, there are selection criteria for transducers, actuators and controllers. In the system simulations presented previously, full state feedback was assumed to be available, meaning that the crane position (x1), velocity (x2), angle (x3) and angular velocity (x4) was assumed to be immediately available as feedback signals for the controller. The actuators, transducers, transmitters and various sensors were also omitted in the simulations. The output of the controllers was normalized for the gantry crane system, as controllers directly output force as control signal. In real world scenarios, however, this is not the case. In order to move the gantry crane, a converter or driver system is necessary, which is usually of second order dynamics. In order to induce force on the mechanical system, actuators are needed, that convert one form of energy into motion. This is usually achieved by rotary AC motors with encoders mounted on them, which convert electric energy to controlled force, by the help of variable frequency drivers. Thus, the crane bridge and trolley position and velocity states can be extracted from the encoders. The controller can either be selected as centralized standalone or as a distributed type controller directly mounted on the drivers, but eventually, must be motion control capable by having fast scan cycle times with high bandwidth. They can pass the generated force reference signal, with upper and lower limits same as driver system limits such as maximum acceleration, speed and current limits, to drivers via digital communication

or analog signals. Due to increased cost, complexity and maintenance, achieving full state feedback is usually not possible in real world scenarios. For measuring angle and angular velocity, feedback state observers can be utilized, providing they sustain good performance levels. Otherwise, they can be measured by transducers such as accelerometer, inclinometer, gyroscope or vision camera. The first three measuring devices usually require direct mounting on the target and cable connections for sending the feedback signal, which is strongly not desired for cranes as they carry payload on their hooks and spreaders. Therefore, these sensors and their cables can easily be damaged during transportation process. Vision camera feedback remains as a viable solution with the advantage of contactless measuring, although this time angle measuring system becomes susceptible to dusty, foggy, snowy weather conditions. Conclusively, a proper evaluation should be done beforehand. As all of the states, namely the payload position, velocity, angle and angular velocity are controlled by crane translating motion along the both cartesian x and y axes, no more actuators than AC motors are required.

CHAPTER 4
RESULTS AND DISCUSSIONS

4.1 Simulation Results without Noise

The mathematical crane model is simulated as an ideal system without noise with respect to the LQR, LQR-PID and LQR-SMC control systems as shown in **Figure 3.5**, **Figure 3.7** and **Figure 3.8**. The results for each state were plotted in the same respective graph in order to elaborate the system responses more accurately. The first four plots in **Figure 4.1**, **Figure 4.2**, **Figure 4.3** and **Figure 4.4** represent the system response with bridge, trolley and payload weights along the x-axis. The last four figures represent the system responses only with the trolley and payload weight along the y-axis.

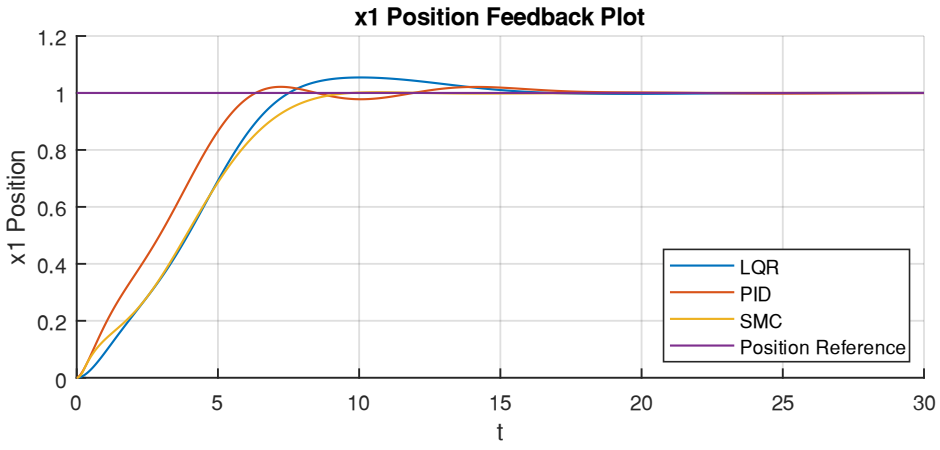

Figure 4.1. x1 position feedback plot for x-axis with no noise

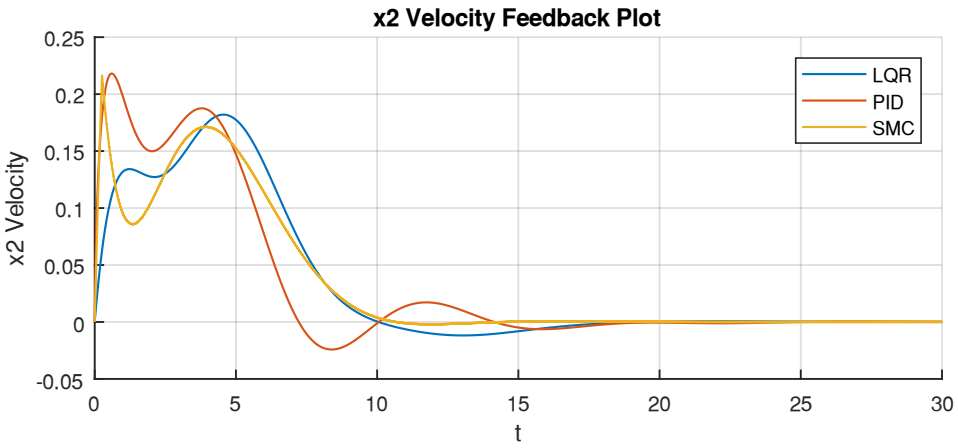

Figure 4.2. x2 velocity feedback plot for x-axis with no noise

Figure 4.3. x3 angle feedback plot for x-axis with no noise

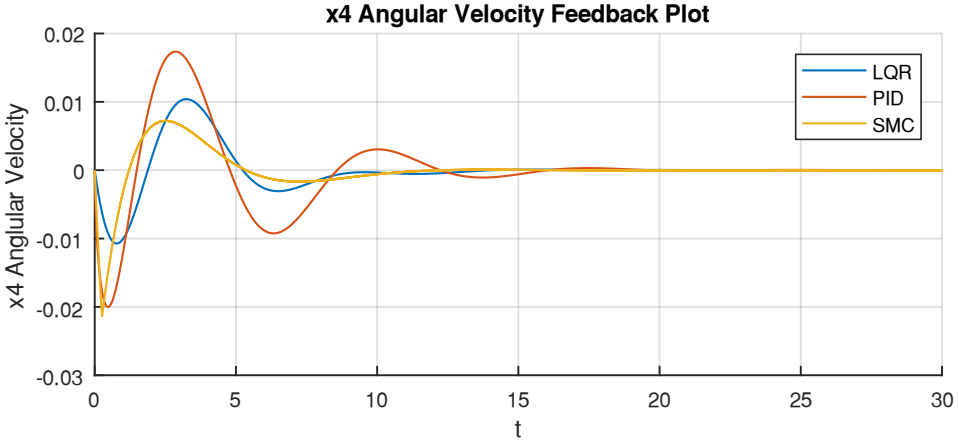

Figure 4.4. x4 angular velocity feedback plot for x-axis with no noise

As seen in **Figure 4.1**, PID has the shortest rise time with 6.3330 seconds, because proportional and adaptive integrator terms provide rapid error correction. It has a position overshoot of 0.0215 meters and a settling time of 14.7410 seconds. SMC, on the other hand, has almost no overshoot with 0.0026 meters, a settling time of 8.4220 seconds and the rise time with 9.7160 seconds. LQR has the highest overshoot with 0.0544 meters. The rise and settling times are 7.5120 and 13.9810 seconds respectively.

Comparing the velocities in **Figure 4.2**, PID has the highest magnitude and change in velocity, which is not ideal for angle deviation. SMC has the smoothest velocity transition, except at the time instant of transition from reaching phase to sliding phase, which should be improved in future work. The angle and angular velocity deviations are highest for the PID case as seen in **Figure 4.3** and **Figure 4.4**. SMC has the best angle and angular velocity control.

The control input signal plot for x-axis for complete simulation time interval is presented in the figure below.

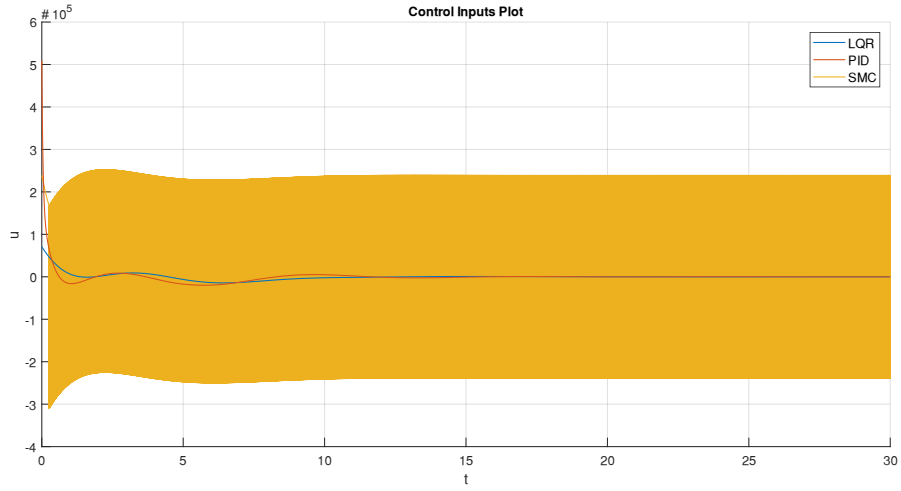

Figure 4.5. Control input signal plot for x-axis with no noise

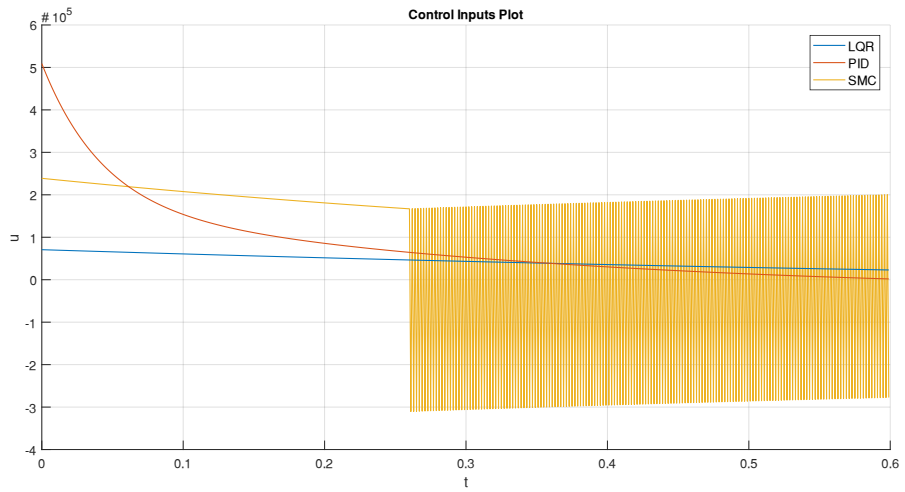

Figure 4.6. Magnified control input signal plot for x-axis with no noise

The main disadvantage of SMC controller can be observed in the control input signal plots above, as the control effort is highest for the SMC controller due to the chattering effect with high signal switching frequency and amplitude. This chattering phenomenon occurs due to the nature of the control input switching mechanism of the sliding mode controller. Therefore, using the SMC controller for real world crane applications as it is, is not feasible. In order to eliminate the chattering effect there are various approaches to take: a quasi sliding mode control law with sigmoid function which is continuous, designing an integral sliding mode controller or designing a super-twisting sliding mode controller. For the last two approaches, the switching control is hidden in the derivatives by using the proper control laws, therefore the actual control signal applied to the plant becomes free of this chattering effect.

The control input signal has a simulation frequency of 1kHz and a peak-to-peak amplitude of around 5×10^5 Newtons, which is not realizable for real cranes as the actuators become saturated, therefore must be selected oversized for the application, which in turn increases the installation and maintenance costs to unrealistically high levels. Hence, a suitable balance between setpoint tracking with unmatched disturbance rejection and control input signal magnitude must be established by iterating the quadratic minimization design process and compromise on robustness must be made. Compromise on robustness against matched uncertainty is not included in this criterion, since SMC guarantees its complete rejection by design.

The previous four plots in **Figure 4.1**, **Figure 4.2**, **Figure 4.3** and **Figure 4.4** represent the system response with bridge, trolley and payload weights along the x-axis. The next four figures represent the system responses only with the trolley and payload weights along the y-axis.

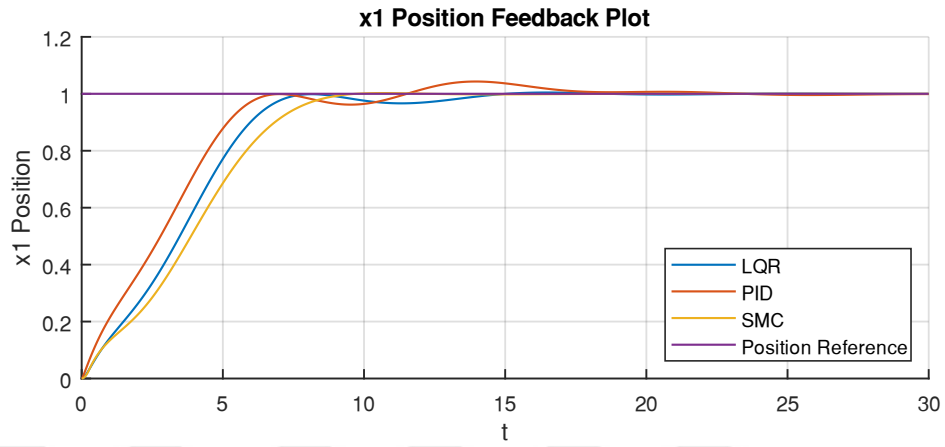

Figure 4.7. x1 position feedback plot for y-axis with no noise

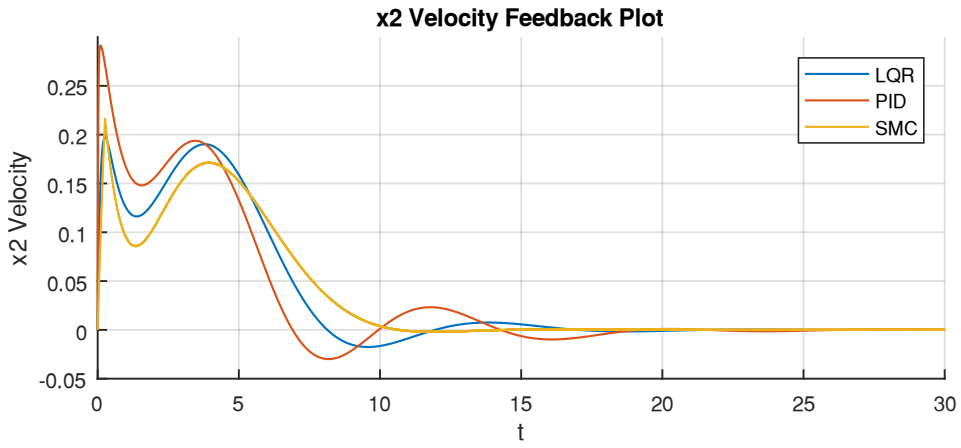

Figure 4.8. x2 velocity feedback plot for y-axis with no noise

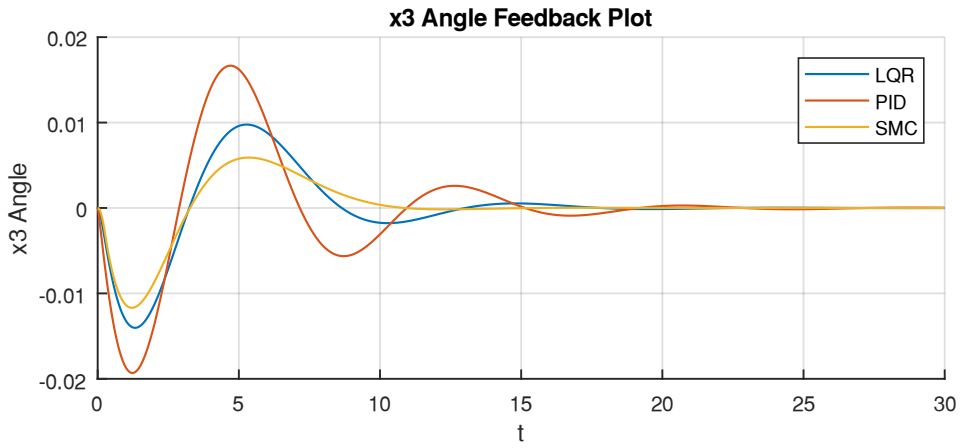

Figure 4.9. x3 angle feedback plot for y-axis with no noise

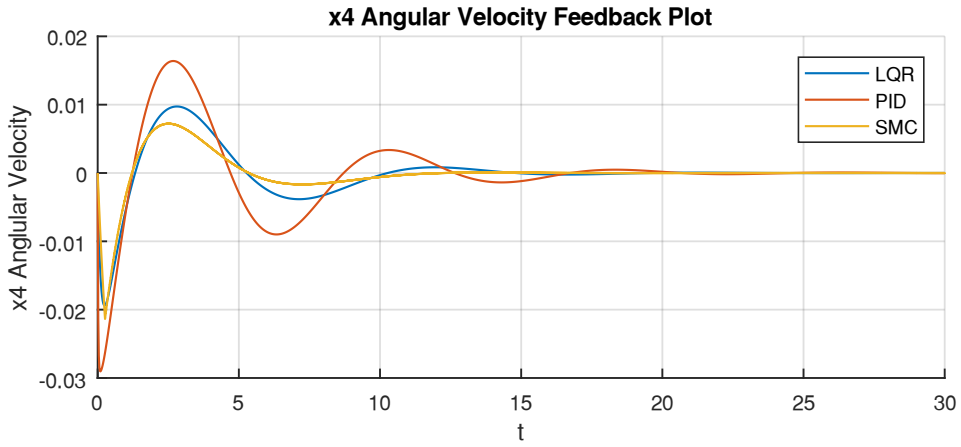

Figure 4.10. x4 angular velocity feedback plot for y-axis with no noise

As seen in **Figure 4.7**, PID has the shortest rise time with 5.9880 seconds, because proportional and adaptive integrator terms provide rapid error correction. It has the highest position overshoot of 0.0290 meters and settling time of 15.7840 seconds. SMC, on the other hand, has almost no overshoot with 0.0026 meters, the lowest settling time of 8.4220 seconds and the rise time with 9.7160 seconds. Please note that after configuring the SMC sliding surface for x-axis they were not changed for the y-axis, so both x and y axes the same switching matrix was used in order to demonstrate the robustness of LQR-SMC controller for the plant parameter variations. Lastly, LQR has the second highest overshoot with 0.0046 meters. The rise and settling times are 15.0470 and 13.1250 seconds respectively.

Comparing the velocities in Figure 4.2, PID has the highest magnitude and change in velocity, which is not ideal for angle deviation. SMC, again, has the smoothest velocity transition, except at the time instant of transition from reaching phase to sliding phase, which should be improved by the application of integral or super-twisting sliding controller in future work. The angle and angular velocity deviations are highest for the PID case as seen in **Figure 4.9** and **Figure 4.10**. SMC has the best angle and angular velocity control.

The control input signal plot for *y*-axis for complete simulation time interval is presented in the figure below.

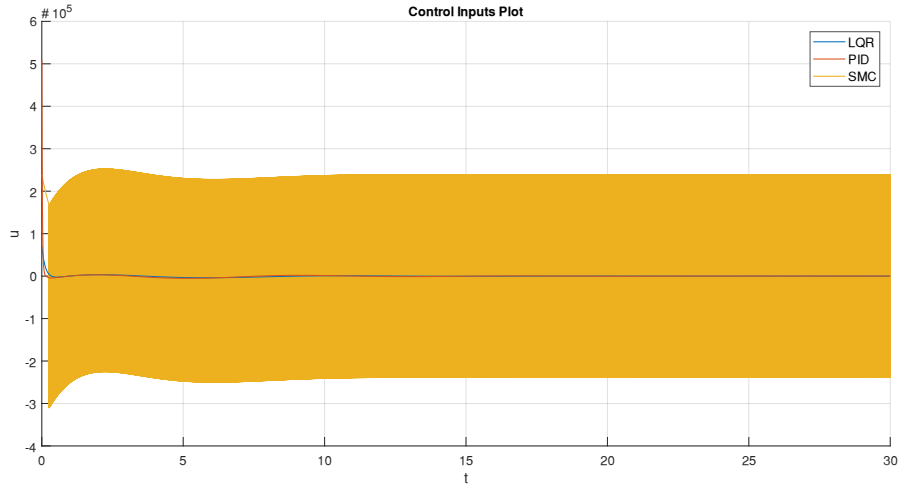

Figure 4.11. Control input signal plot for y-axis with no noise

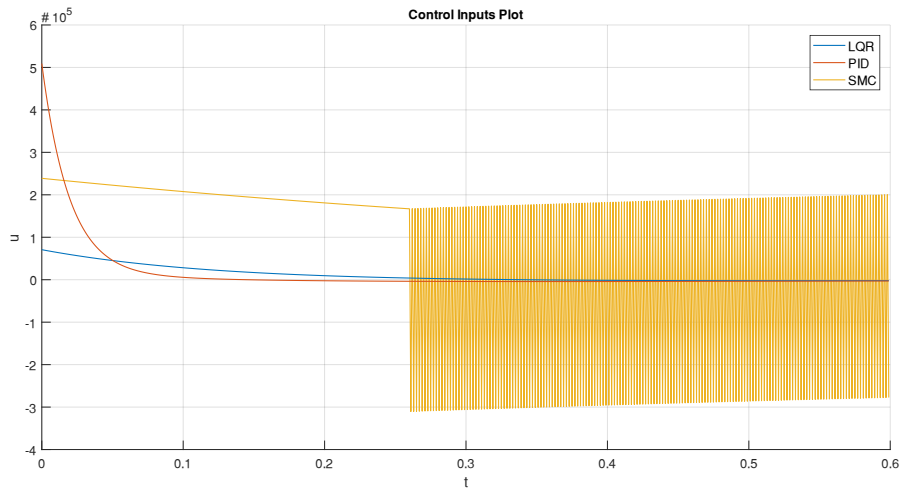

Figure 4.12. Magnified control input signal plot for y-axis with no noise

In order to compare the performances of the controllers, the mean square error (MSE) values as calculated with the formula $MSE = \frac{1}{n}\sum_{i=1}^{n}(r_1 - x_1)^2$ for x_1 position feedback and r_1 position reference are tabulated below:

Table 4.1. MSE values for systems with no noise

	MSE Values x-axis	**MSE Values for y-axis**
LQR Controller	0.0908	0.0776
LQR-PID Controller	0.0641	0.0573
LQR-SMC Controller	0.0871	0.0871

As seen in the table above there is actually room for improvement of the SMC controller MSE values through decreasing the rise time.

4.2 Simulation Results with Integrated White Noise

The simulations with integrated white noise in the control input path is shown in the figures below. The results for each state were plotted in the same respective graph in order to elaborate the system responses more accurately. The first four plots represent

the system response with bridge and trolley weights along the x-axis. The last four figures represent the system responses only with the trolley weight along the y-axis.

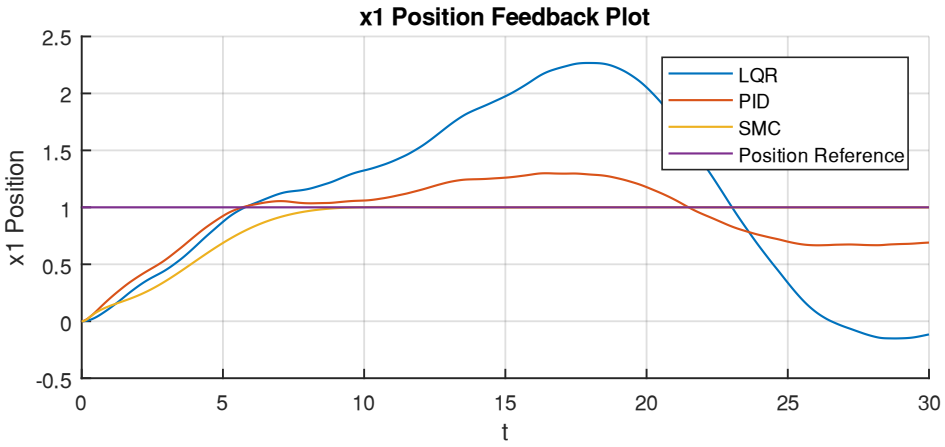

Figure 4.13. x1 position feedback plot for x-axis with white noise

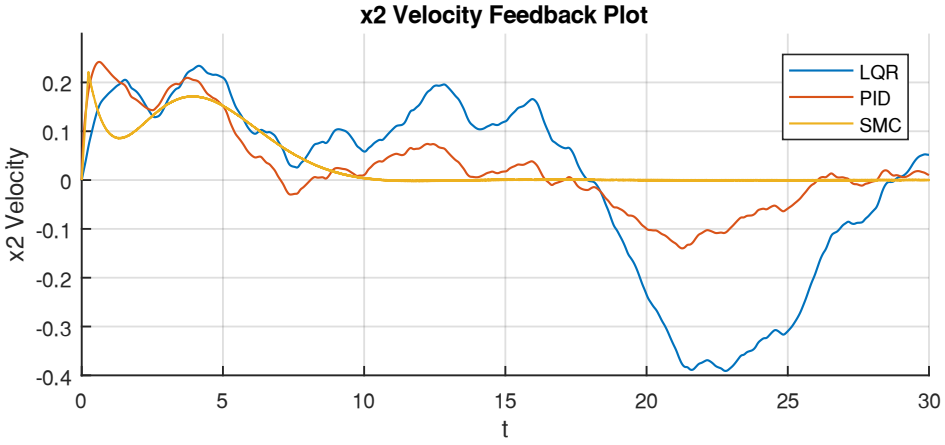

Figure 4.14. x2 velocity feedback plot for x-axis with white noise

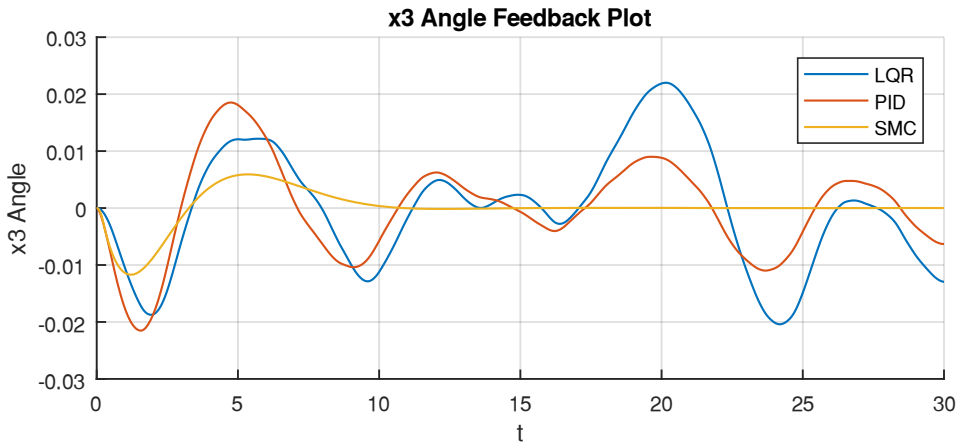

Figure 4.15. x3 angle feedback plot for x-axis with white noise

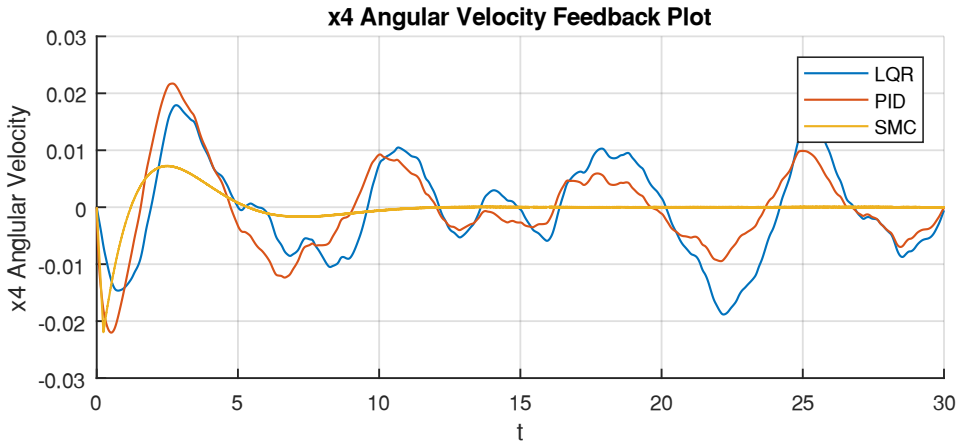

Figure 4.16. x4 angular velocity feedback plot for x-axis with white noise

As seen in **Figure 4.13**, SMC shows the best performance in terms of disturbance rejection. The peak values for LQR, PID and SMC are 2.2673, 1.2991 and 1.0029 meters respectively. SMC controller completely attenuates the uncertainty in all of the system states. The angle and angular velocity control remain the smoothest for SMC controller.

The control input signal plot for x-axis for complete simulation time interval is presented in the figure below.

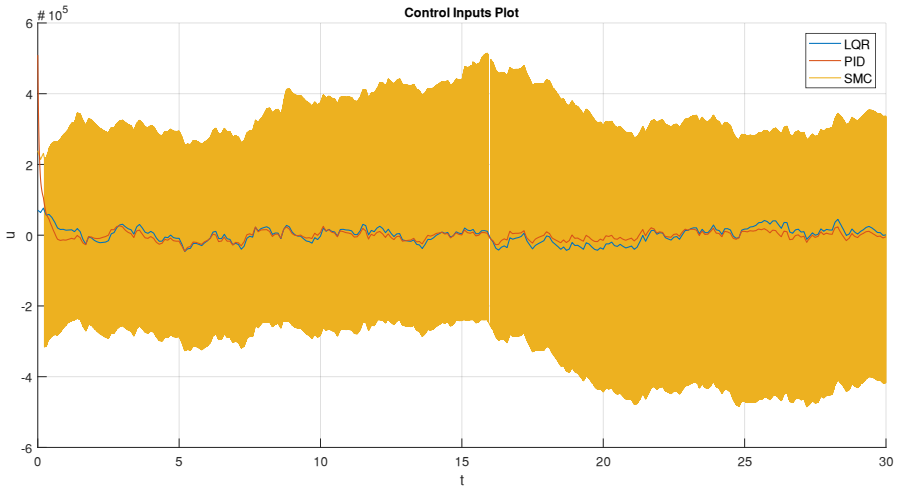

Figure 4.17. Control input signal plot for x-axis with integrated white noise

The previous plots represent the system responses and control action with bridge, trolley and payload weights along the x-axis. The next five figures represent the system responses and control action only with the trolley and payload weights along the y-axis.

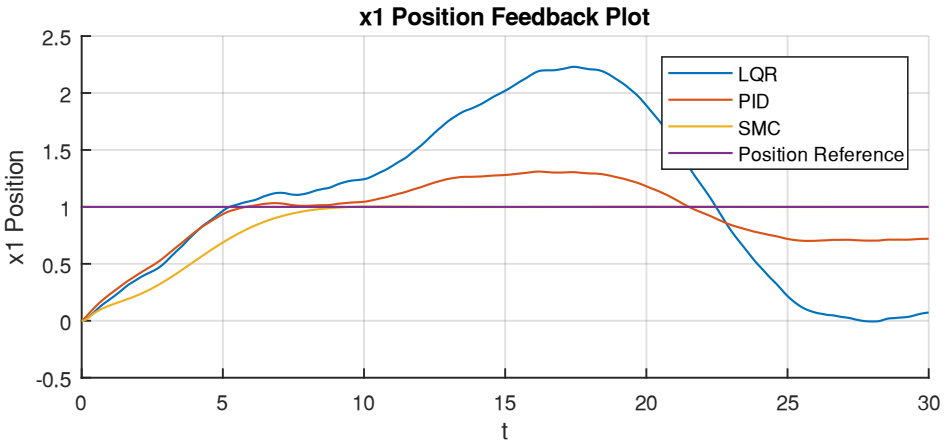

Figure 4.18. x1 position feedback plot for y-axis with white noise

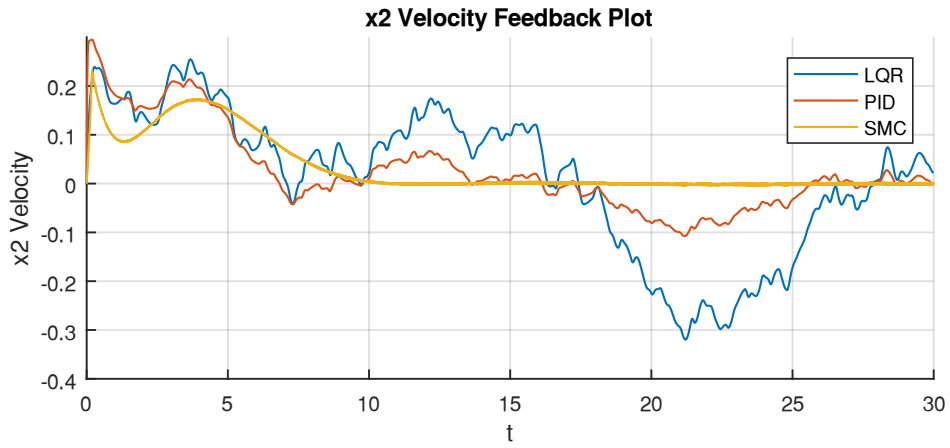

Figure 4.19. x2 velocity feedback plot for y-axis with white noise

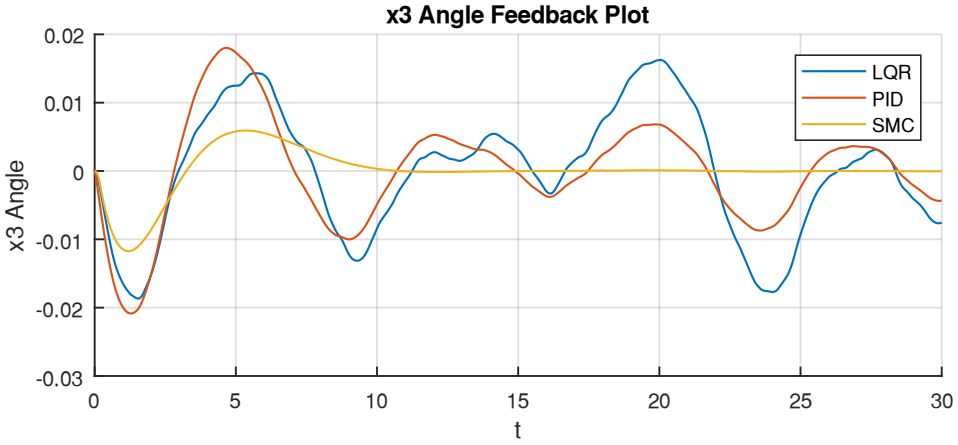

Figure 4.20. x3 angle feedback plot for y-axis with white noise

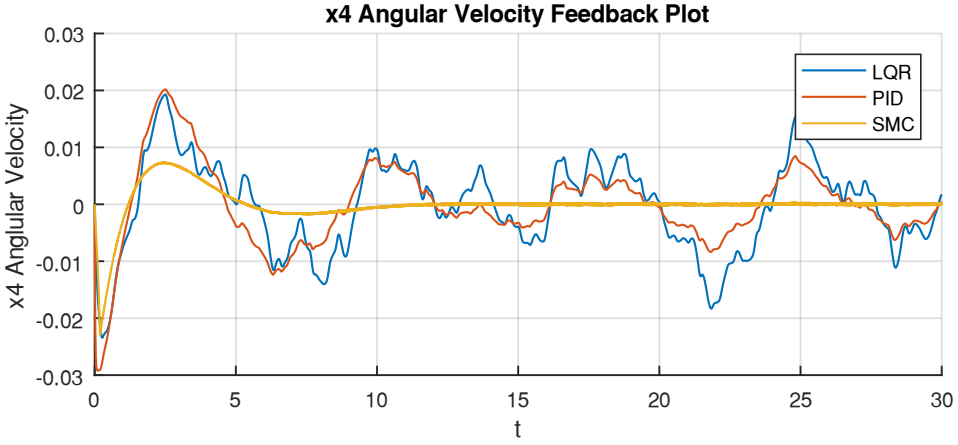

Figure 4.21. x4 angular velocity feedback plot for y-axis with white noise

As seen in **Figure 4.18**, SMC again shows the best performance in terms of disturbance rejection. The peak values for LQR, PID and SMC are 2.2298, 1.3100 and 1.0029 meters respectively.

The control input signal plot for y-axis for complete simulation time interval is presented in the figure below.

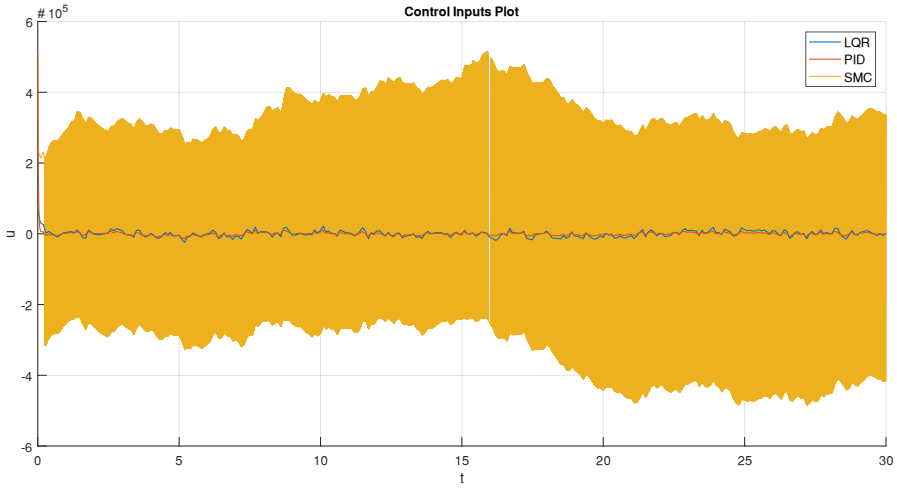

Figure 4.22. Control input signal plot for y-axis with integrated white noise

The mean square error (MSE) values representing the difference between x_1 position feedback and r_1 position reference are tabulated below:

Table 4.2. MSE values for systems with integrated white noise

	MSE Values x-axis	**MSE Values for y-axis**
LQR Controller	0.6172	0.5521
LQR-PID Controller	0.1003	0.0935
LQR-SMC Controller	0.0869	0.0869

As seen in the table above SMC controller gives satisfactory performance comparing the transient, steady-state and MSE characteristics. Additionally, since the PID designed in this study is a modified PID in order to avoid overshoot, its MSE performance is superior than standard PID controller. As the magnitude of

uncertainties in the system increase, the difference between PID and SMC will decrease for the advantage of SMC.

4.3 Simulation Results with Sinusoidal Noise

The simulations with sinusoidal noise of amplitude 1×10^4 and of frequency $0.05\ Hz$ in the control input path is shown in the figures below. The results for each state were plotted in the same respective graph in order to elaborate the system responses more accurately.

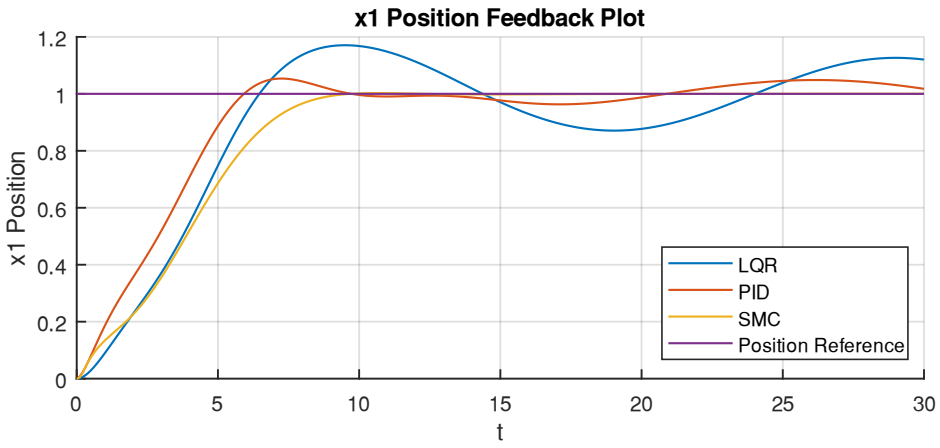

Figure 4.23. x1 position feedback plot for x-axis with sinusoidal noise

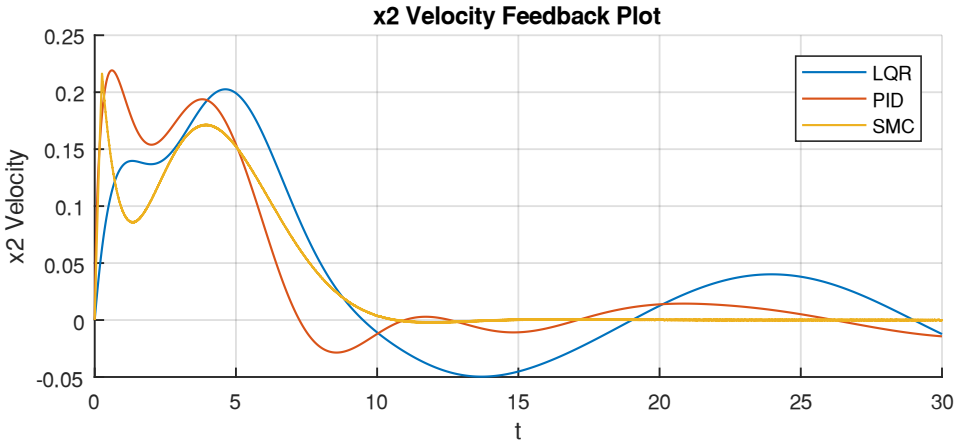

Figure 4.24. x2 velocity feedback plot for x-axis with sinusoidal noise

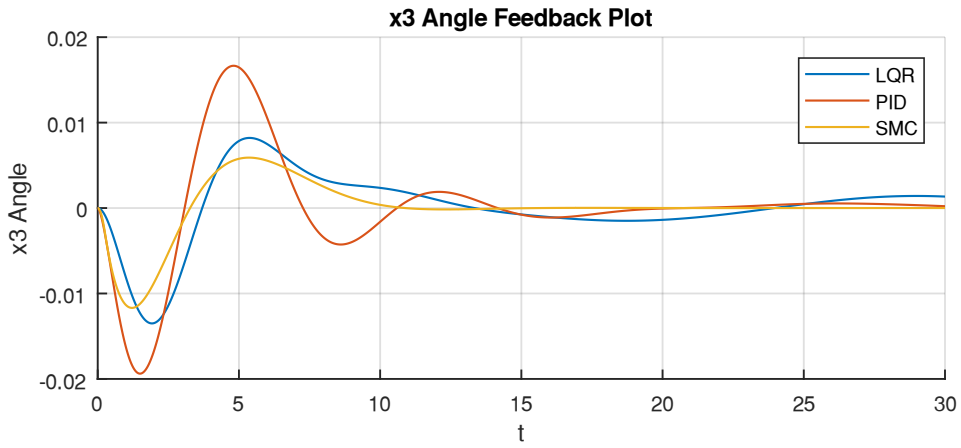

Figure 4.25. x3 angle feedback plot for x-axis with sinusoidal noise

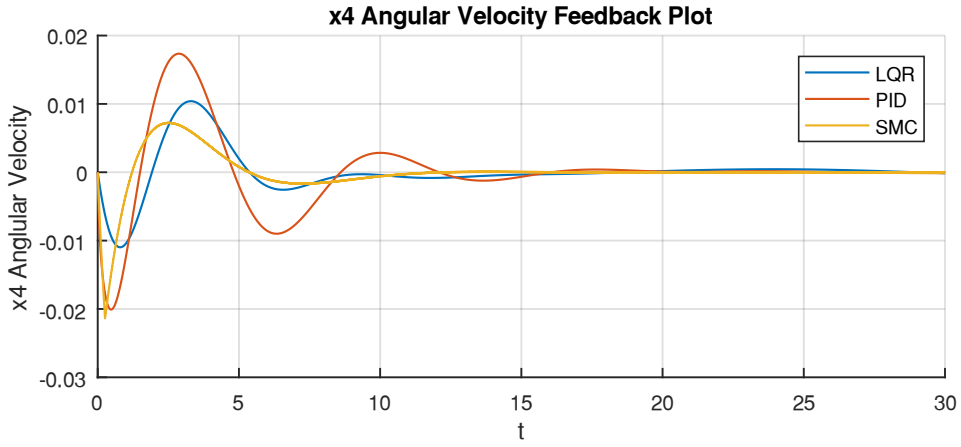

Figure 4.26. x4 angular velocity feedback plot for x-axis with sinusoidal noise

As seen in the figures SMC shows the best performance in terms of disturbance rejection. SMC controller completely attenuates the matched uncertainty in all of the system states and angle and angular velocity control remain the smoothest. PID controller has better position control than LQR controller, but the angle and angular deviation is higher.

The control input signal plot for x-axis for complete simulation time interval is presented in the figure below.

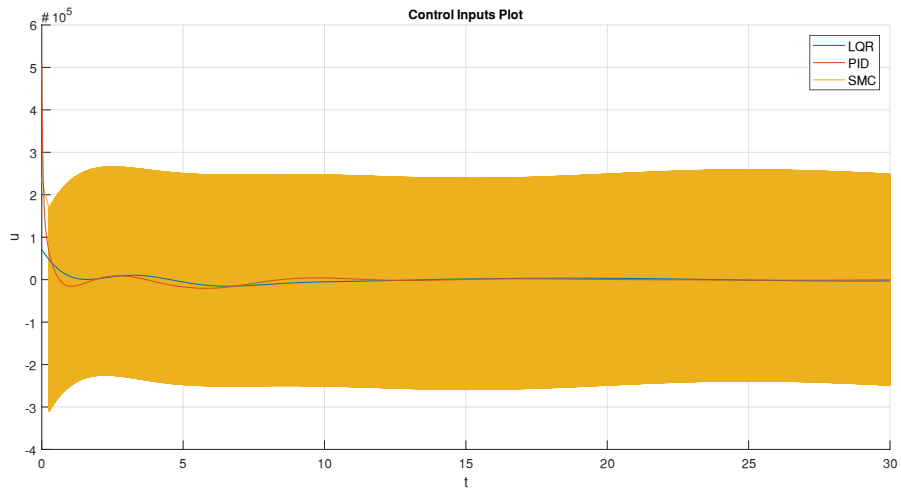

Figure 4.27. Control input signal plot for x-axis with sinusoidal noise

The next figures show the system states for the y-axis with only the trolley and payload weights.

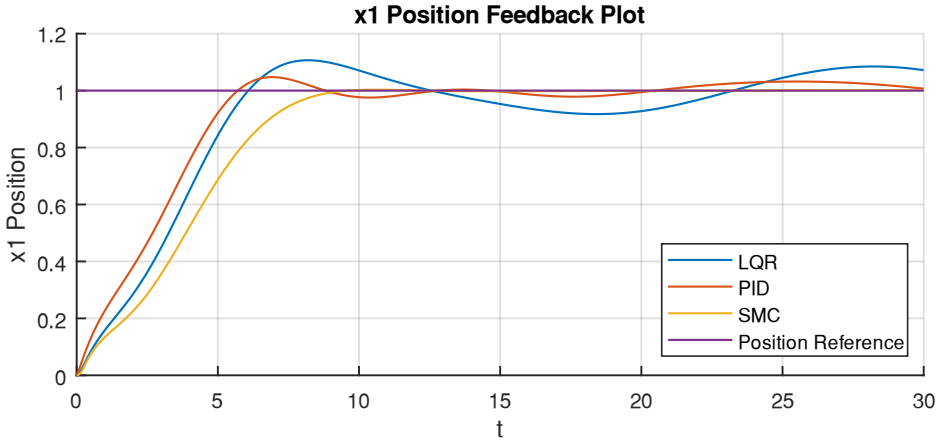

Figure 4.28. x1 position feedback plot for y-axis with sinusoidal noise

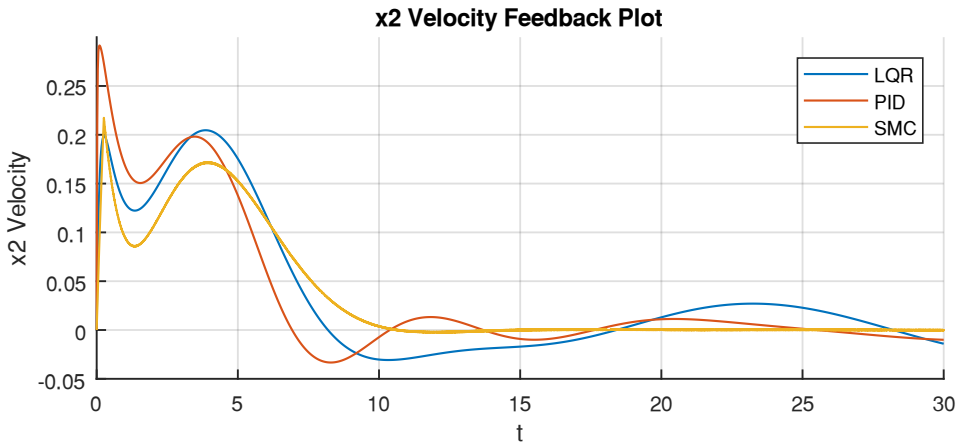

Figure 4.29. x2 velocity feedback plot for y-axis with sinusoidal noise

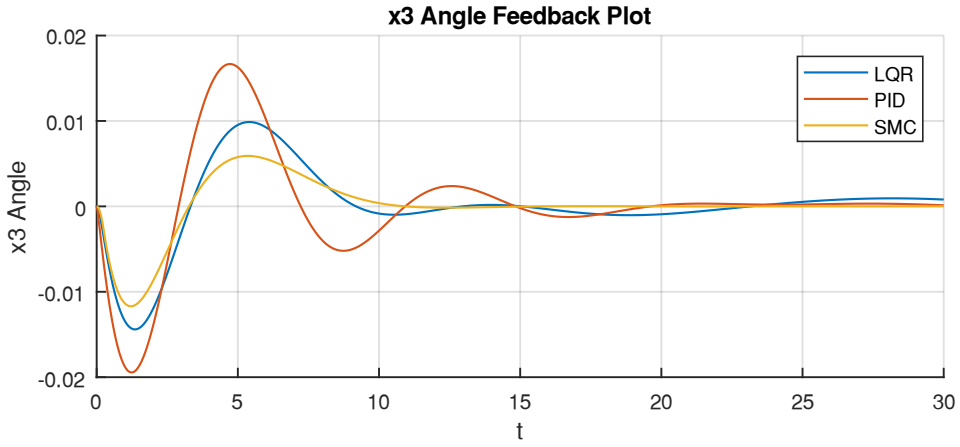

Figure 4.30. x3 angle feedback plot for y-axis with sinusoidal noise

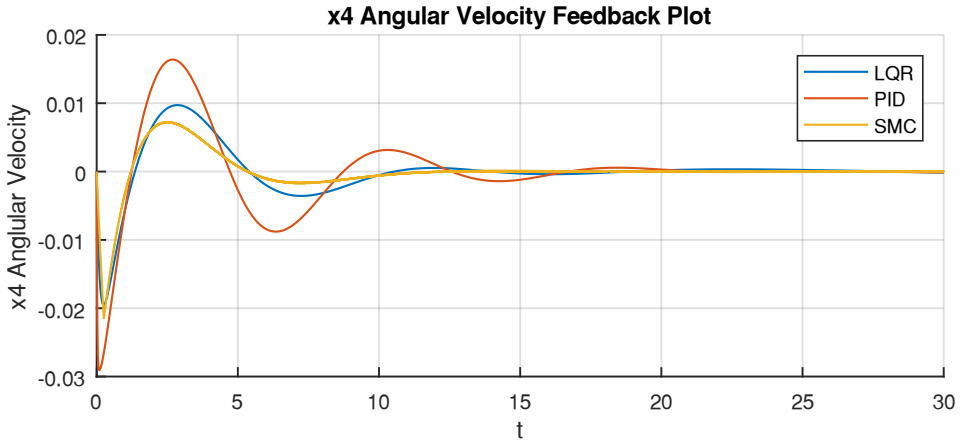

Figure 4.31. x4 angular velocity feedback plot for y-axis with sinusoidal noise

The control input signal plot for y-axis for complete simulation time interval is presented in the figure below.

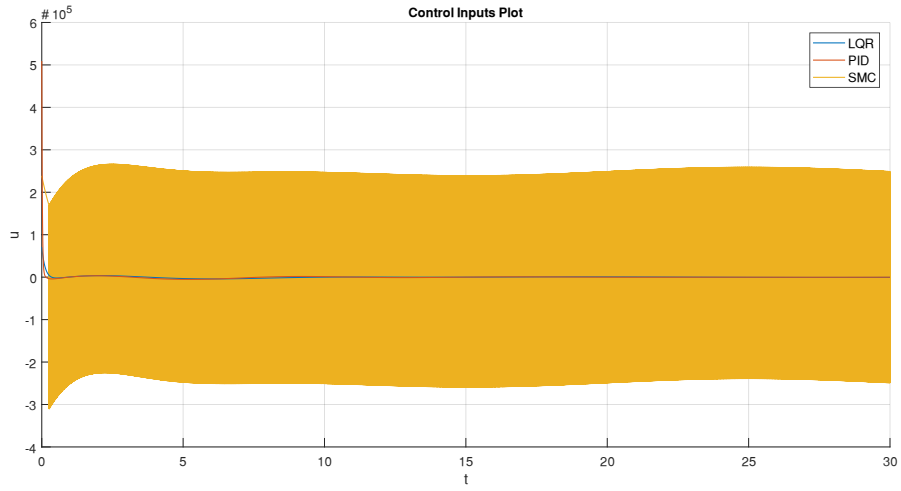

Figure 4.32. Control input signal plot for x-axis with sinusoidal noise

The mean square error (MSE) values representing the difference between x_1 position feedback and r_1 position reference are tabulated below:

Table 4.3. MSE values for systems with sinusoidal noise

	MSE Values x-axis	**MSE Values for y-axis**
LQR Controller	0.0948	0.0788
LQR-PID Controller	0.0637	0.0589
LQR-SMC Controller	0.0871	0.0871

As **Table 4.1**, **Table 4.2** and **Table 4.3** are inspected together, it can be seen that the MSE values for SMC are constant at around 0.0871, whereas the values for LQR and PID controllers change widely. This proves the performance of LQR-SMC as disturbance rejecting robust controller for both marched and unmatched uncertainties. Further decreasing the SMC rise time will close this MSE performance gap.

CHAPTER 5
CONCLUSION AND FUTURE WORK

5.1 Conclusion

As studied in the results and discussions above, all three controllers show good performance in no noise simulation. LQR is expected to overshoot by some percentage in regard to the selection of the cost matrices. PID on the other hand, normally is expected to show higher overshoot than LQR, but since in this study a customized type PID with adaptive integral multiplier is used, the overshoot is reduced very significantly. SMC as expected shows stable operation with no overshoot. For simulations with uncertainties, SMC control system exhibits complete matched uncertainty rejection when it is introduced in the control input path and conditional unmatched uncertainty rejection when it is introduced in the plant system matrix. The transient and steady-state characteristics for all three controllers can be manipulated iteratively during the LQR design process, as all of the control systems use state feedback in the signal return path, further improving the system responses. The LQR controller has the worst disturbance rejection since it only uses feedback gains. PID on the other hand, have integrator and derivative terms and SMC has high control signal frequency that inherit robustness. As indicated above, the introduction of adaptive integrator multiplication coefficient to the PID controller again improved the transient and steady-state characteristics, by not compromising the rise time at the same time decreasing the overshoot very significantly. The SMC controller naturally has the matched uncertainty rejection by its nature, but with the introduction of LQR design to the SMC, it also becomes robust to the unmatched uncertainty in the plant characteristic equation, as the motion coordinates switch from x-axis to y-axis.

5.2 Future Work

The control schemes explained above can be applied to real world cranes. In order to achieve this motor driver, motor and transmission should also be taken into consideration by including them in the overall crane system model.

In real cranes the bridge and trolley can move separately along different axes. For example, if both bridge and trolley move along the x-axis, only the trolley moves along the y-axis, since trolley is placed on top of bridge. Therefore, bridge carries trolley's weight while moving along the x-axis.

Although the SMC controller exhibits superior performance in terms of disturbance rejection, transient characteristics and setpoint tracking, it introduces serious chattering problems due to control signal switching. This can be remedied by the introduction of integral or twisting sliding modes to the controller. The rise time to the position setpoint can also be improved by iterating LQR the design process for SMC.

REFERENCES

[1] Ogata, K., (2010). 5 Ed., *Modern Control Engineering*, Pearson Education: New Jersey.

[2] Aström K.J., Hagglund T., (2006). 1 Ed., *Advanced PID Control*, ISA Instrumentation, Systems and Automation Society: NC.

[3] Shtessel Y., Edwards C., Fridman L. and Levant A., (2014). 1 Ed., *Sliding Mode Control and Observation*, Birkhäuser, Springer Science: MD.

[4] Utkin V., Guldner J., Shi J., (2009). 2 Ed., *Sliding Mode Control in Electro-Mechanical Systems*, CRC Press: NW.

[5] Morin D., (2007). 1 Ed., *Introduction to Classical Mechanics*, Cambridge University Press: Cambridge.

[6] Herbert G., Poole C.P., Safko J.L., (2001). 3 Ed., *Classical Mechanics*, Addison Wesley: NY.

[7] Hibbeler R.C., (2013). 13 Ed., *Engineering Mechanics Dynamics*, Pearson Education: New Jersey.

[8] Franklin G.F., Powell J.D., Naeini A.E., (2009). 6 Ed., *Feedback Control of Dynamic Systems*, Pearson Education: England.

[9] Anton H., Rorres C., (2014). 11 Ed., *Elementary Linear Algebra*, Wiley: USA.

[10] Giancoli D.C., (2014). 4 Ed., *Physics for Scientists & Engineers with Modern Physics*, Pearson Education: England.

[11] McClellan J.H., Schafer R.W., Yoder M.A., (2017). 2 Ed., *DSP First*, Pearson Education: England.

[12] Castillo-García P., Hernandez L.E.M., Gil P.G., (2017), Chapter 7 – Sliding Mode Control, *Indoor Navigation Strategies for Aerial Autonomous Systems*, pp 157-179, Elsevier.

[13] Vandiver K., (2011), An Introduction to Lagrange Equations, *2.003SC/1.053J Engineering Dynamics*, MIT OpenCourseWare.

[14] Young K.D., Utkin V.I., Özgüner Ü., (1999). A Control Engineer's Guide to Sliding Mode Control, *IEEE Transactions on Control Systems Technology*, Vol. 7, No. 3, pp 328-342.

[15] Olsson H., Aström K.J., et al., (1998), Friction Models and Friction Compensation, *European Journal of Control*, Vol. 4, Iss. 3, pp 176-195.

[16] Ramli L., et al., (2017), Control Strategies for Crane Systems, *Journal of Mechanical Systems and Signal Processing*, Elsevier.

[17] Abdelrahman E.M., et al., (2001), Dynamics and Control of Cranes: A Review, *Journal of Vibration and Control*, Sage Publications.

[18] Neupert J., et al., (2010), Tracking and Anti-sway control for boom cranes, *Control Engineering Practice*, Elsevier.

[19] Singhose W., (2009), Command Shaping for Flexible Systems: A Review of the First 50 Years, *International Journal of Precision Engineering and Manufacturing*, Vol. 10, No. 4, pp 153-168.

[20] Kim Y., et al., (2004), Anti-sway Control of Container Cranes: Inclinometer, Observer and State Feedback, *International Journal of Control, Automation and Systems*, Vol. 2, No. 4, pp 435-449.

[21] Raubar E., Vrancic D., (2012), Anti-sway System for Ship-to-Shore Cranes, *Journal of Mechanical Engineering*, 58(2021)5, pp 338-344.

[22] Golovin I., Palis S., (2019), Robust control for active damping of elastic gantry crane vibrations, *Mechanical Systems and Signal Processing*, 121 (2019), pp 264-278.

[23] Tuan L., et al., (2018), Adaptive neural network sliding mode control of shipboard container cranes considering actuator backlash, *Mechanical Systems and Signal Processing*, 112 (2018), pp 233-250.

[24] Maghsoudi M., et al., (2015), An optimal performance control scheme for a 3D crane, *Mechanical Systems and Signal Processing*, Vol. 66-67, pp 756-768.

[25] Knierim K.L., et al., (2010). Flatness Based Control of a 3-DOF Overhead Crane with Velocity Controlled Drives, *5th IFAC Symposium on Mechatronic Systems*, 363-368.

[26] Chaturvedi N.A., et al., (2011). Nonlinear Dynamics of 3D Pendulum, *Journal of Nonlinear Science*, 21 3-32.

[27] Chaturvedi N.A., et al., (2008). Stabilization of a 3D axially symmetric pendulum, *Automatica*, 44 2258-2265.

[28] Piriou J., (2010). *Anti-Sway: controlling the swaying of the load*, Optimising production methods, Schneider-Electric.

[29] Gustafsson T., Heidenback C., (2002). Automatic Control of Unmanned Cranes at the Pasir Panjang Terminal, *Proceedings of the 2002 IEEE International Conference on Control Applications*, 180-185.

[30] Catalan J., (2018), Design and calculation of the structure of a gantry crane with 50 tons of capacity and 50 meters of span, *Convocatoria de defensa*, Universitat Politecnica De Valencia.

[31] Alkin C., et al., (2005), Solid Modelling and Finite Element Analysis of an Overhead Crane Bridge, *Acta Polytechnica*, Vol. 45, No. 3/2005, pp 61-67.

[32] Furat M., Eker İ., (2012). Experimental Evaluation of Sliding-Mode Control Techniques, *Çukurova University Journal of the Faculty of Engineering and Architecture*, 27(1), pp 23-37.

[33] Çandır E., (2014). *Cascaded Proxy-Based Sliding Mode Control Enhanced with Disturbance Observer for the Stabilization and Control of a Gun-Turret Platform*, Thesis, Middle East Technical University.

[34] Villacres J., et al., (2016), Controllers Comparison to Stabilize a Two-wheeled Inverted Pendulum: PID, LQR and Sliding Mode Control, *International Journal of Control Systems and Robotics*, Vol. 1, pp 29-36.

[35] Barbosa F.D.S., et al., (2018). Sliding Mode Control with Linear Quadratic Regulator Augmented with Integrators Applied to a 2DOF Helicopter, *XXII Congresso Brasileiro de Automática João Pessoa Brasil*, 9-12.09.2018.

[36] Herrera M., et al., (2017). A Blended Sliding Mode Control with Linear Quadratic Integral Control based on Reduced Order Model for a VTOL System, *Proceedings of the 14th International Conference on Informatics in Control, Automation and Robotics (ICINCO)*, Vol. 1, pp 606-612.